# Patient-calibrated agent-based modelling of ductal carcinoma in situ (DCIS) I: Model formulation and analysis

Paul Macklin [1,2,3], Mary E. Edgerton [4], Alastair Thompson [4,5], Vittorio Cristini [3,6]

**Abstract**

Ductal carcinoma in situ (DCIS)–an important precursor to invasive breast cancer–is typically diagnosed as microcalcifications in mammograms. However, the effective use of mammograms and other patient data to plan treatment has been restricted by our limited understanding of DCIS growth and calcification.

We develop a mechanistic, agent-based model of DCIS that is broadly applicable beyond breast cancer. The motion of each cell is determined by a balance of adhesive, repulsive, and motile forces. Interaction forces are governed by potential functions that can model heterophilic and homophilic adhesion, interaction between cells of unequal size and phenotype, and interaction with a basement membrane. Each cell has a phenotypic state that is governed by exponentially-distributed random variables. This is a natural generalisation of prevalent models, and provides a rigorous way to vary transition probabilities with variable time step sizes and the microenvironment. Each agent has a detailed "submodel" of the cell volume changes during proliferation and necrosis (including the first model for the fast time scale processes of swelling and lysis), and we are the first to account for cell calcification. We simulate the microenvironment through coupled reaction-diffusion equations. The result is a modelling framework that is well-suited to investigating the biophysical mechanisms of DCIS growth and calcification. An analysis of the model's volume-averaged behaviour yields new insight on the relationship between intraductal oxygen levels, proliferation, and heterogeneous cell signalling; we test these ideas against patient immunohistochemistry data.

This paper is the first in a two-part series on DCIS modelling. In Part II, we use our analysis to develop a patient-specific model calibration protocol, simulate DCIS in a virtual patient, generate macroscopic predictions on DCIS microstructure and clinical progression, and test these against large, independent sets of clinical data.

*Key words:* agent-based modelling, tumour simulation, nonhomogeneous Poisson processes, necrosis, biomechanics, calcification, ductal carcinoma in situ (DCIS)
*1991 MSC:* 65C20, 92B05, 92C05

# 1 Introduction

Ductal carcinoma in situ (DCIS), a type of breast cancer where growth is confined within the breast ductal/lobular units, is the most prevalent precursor to invasive ductal breast cancer (IC). Breast cancer is the second-leading cause of death in women in the United States. The American Cancer Society predicted that 50,000 new cases of DCIS alone (excluding other forms of pre-invasive change such as lobular carcinoma in situ) and 180,000 new cases of IC would be diagnosed in 2007 (Jemal et al., 2007; American Cancer Society, 2007). Co-existing DCIS is expected in 80% of IC, or 144,000 cases (Lampejo et al., 1994). While DCIS itself is not life-threatening, it is a very important precursor to IC because (1) it can be treated and (2) if left untreated, it has a high probability of progression to IC, which is a deadly disease (Page et al., 1982; Kerlikowske et al., 2003; Sanders et al., 2005). While the detection and treatment of DCIS have greatly improved over the last few decades, problems persist. DCIS can be difficult to detect by mammography, the principle modality in breast screening, or to distinguish from other aberrant lesions (Venkatesan et al., 2009). This can lead to "false positives" of DCIS and overtreatment, including unnecessary surgery. On the other hand, even in cases where DCIS excision is truly warranted, multiple procedures may be required to fully eliminate all DCIS, due to the differences between the pre-operative estimated and actual resected histopathology findings (e.g., of the tumour size and shape) (Cheng et al., 1997; Silverstein, 1997; Cabioglu et al., 2007; Dillon et al., 2007). Hence, a solid scientific understanding of DCIS progression is required to improve clinical decision making.

There are many open questions on DCIS biology which contribute to the current uncertainty in clinical practice. How does DCIS progress from a few proliferating cells to detectable lesions potentially including microcalcifications? How do heterogeneities in cell mechanics and other phenotypic characteristics give rise to specific DCIS morphologies? Is the gap that is often observed between the tumour's viable rim and the necrotic core simply an artifact of histologic preparation, or is it indicative of further biomechanical processes? Can

*Email address:* macklin@maths.dundee.ac.uk (Paul Macklin).

*URL:* http://www.maths.dundee.ac.uk/macklin (Paul Macklin).

[1] Corresponding author

[2] Division of Mathematics, University of Dundee, Dundee, Scotland, UK

[3] Formerly of: School of Biomedical Informatics, University of Texas Health Science Center, Houston, TX, USA

[4] M.D. Anderson Cancer Center, Houston, TX, USA

[5] Department of Surgery and Molecular Oncology, University of Dundee, Dundee, Scotland, UK

[6] Departments of Pathology and Chemical Engineering, University of New Mexico, Albuquerque, NM, USA

observations from immunohistochemistry (IHC) and histopathology images be used to estimate important physiological constants? Conversely, can mathematical modelling provide new insight on interpretting these data? What is the relationship between the microcalcifications observed in mammography and tumour morphology? How can we calibrate patient-specific models to limited and often noisy histopathologic data, often from only a single time point?

These clinically-pertinent scientific questions motivate our model development. Mathematical modelling has already seen use in understanding and predicting the growth of DCIS or its approach towards a steady state. Franks et al. (2003a,b, 2005) and Owen et al. (2004) have used continuum models to investigate tumour growth in breast ducts, including the impact of volume loss in the necrotic core, ductal expansion, and the influence of basement membrane (BM) adhesion (Franks et al., 2003a,b, 2005; Owen et al., 2004); this work can be traced to a long history of work by Ward and King (e.g., Ward and King (1997)) that includes model parameterisation by matching to experiments. Rejniak and co-workers applied an immersed boundary method to individual polarised cells; their model was able to reproduce several complex DCIS sub-types (Rejniak, 2007; Rejniak and Dillon, 2007; Rejniak and Anderson, 2008a,b). More recently, Norton et al. (2010) conducted a similar investigation of the relationship between polarised cell adhesion, intraductal pressure, and DCIS morphology in 2D using a lattice-free agent model and were able to produce nontrivial tumour microstructures (e.g., cribriform patterns). Gatenby et al. (2007), Silva et al. (2010), and Smallbone et al. (2007) have investigated the role of hypoxia, glycolysis, and acidosis in DCIS evolution in 2D and 3D using cellular automata (CA) methods by including detailed metabolic sub-models. Bankhead III et al. (2007) conducted early 3-D simulations of tumour cell heirarchy using CA techniques. Sontag and Axelrod (2005) combined population-scale models with machine learning techniques and statistical analyses to postulate new hypotheses on DCIS mutation pathways from benign precursors, while Enderling et al. (2006, 2007) studied DNA mutation within DCIS and recurrence (particularly following radiation therapy) using continuum and CA methods. Mannes et al. (2002) used CA methods to investigate Pagetoid spread.

All this work has provided a degree of insight into DCIS, but has not fully answered the questions we posed. Typical CA methods cannot accurately model cell mechanics, particularly proliferation by tumour cells when fully surrounded by other cells. Such proliferation, which is regularly observed in DCIS immunohistochemistry, can only be approximated in CA methods by introducing complex, often phenomenological rules to push multiple cells through the simulated domain. Population-based ordinary differential equation (ODE) models do not account for spatial heterogeneity and hence cannot investigate the impact of heterogeneous mechanics, substrate transport, and their interaction. To date, none have modelled the process of microcalcification, and

existing "sub-models" of necrosis have been simple volume loss terms, and have not considered the individual effects of cell swelling and lysis. Indeed, many prevalent models do not include necrosis. The work by Norton et al. (2010) shows promise, but it has yet to predict tumour biophysics as *emergent phenomena* because it imposed many of its mechanical, proliferation, viable rim size, and apoptosis properties *a priori* as algorithmic rules. The detailed morphological model of Rejniak and colleagues has produced impressive results, but faces computational limits when applied to large numbers of cells. Continuum models can overcome these limits, but calibration to molecular- and cell-scale data is not straightforward, particularly for phenomenological "lumped" parameters (Macklin et al., 2010b). We are currently approaching this issue as a multiscale information flow, by upscaling calibrated cell-scale models to the continuum scale (Edgerton et al., 2011). See also the discussion in Cristini and Lowengrub (2010) and recent multiscale modelling reviews (Deisboeck et al., 2010; Lowengrub et al., 2010). To our knowledge, there has been no prior patient-specific calibration to the proliferative and apoptotic indices generally measured in breast biopsies at any scale of modelling.

We presently develop a lattice-free, agent-based cell model that can be applied to many problems, exemplified by DCIS. The cells (agents) are modelled as objects subject to a balance of adhesive, repulsive, and motile forces that determine their motion. Cell-cell and cell-basement membrane interaction mechanics are modelled using potential functions that can account for finite interaction distances, both heterophilic and homophilic adhesion, uncertainty in cell morphology and position, and interaction between cells of variable sizes and types. We introduce a level set formulation of the basement membrane morphology that is well-suited to future deformation modelling, and provides a generalised framework for the exchange of forces between discrete cell objects and extended macroscopic objects with nontrivial geometries.

Each cell is endowed with a phenotypic state, and phenotypic transitions are governed by exponentially-distributed random variables that depend upon the cell's internal state and the local microenvironment. This modelling choice is consistent with experimental biology dating back as far as the 1970s (e.g, Smith and Martin (1973)), is a natural extension of prevalent phenotypic transition models in widespread use today, provides a rigorous method to vary the model's probabilities with the microenvironment and with variable time step sizes (e.g, those arising from numerical stability criteria), and lends itself to mathematical analysis.

Our choice of functional relationship between the quiescent-to-proliferative phenotypic transition rate and oxygen availability yields predictions that we test quantitatively against actual breast patient data. We include detailed "sub-models" of cell volume change during proliferation and necrosis (including the effects of swelling and lysis), which are able to predict subtle mi-

crostructures in the viable rim-necrotic core boundary for the first time, as well as the important impact of mechanical relaxation by lysing cells in the necrotic core. Our model is the first to investigate the development of cellular calcifications towards a clinically-detectable state. We couple the agents to the microenvironment in a composite modelling framework by solving continuum reaction-diffusion equations for substrates that are altered by the cells. To make the model predictive, we constrain all major model parameters by surveying a broad swath of the experimental and theoretical biology literature through a "mathematical lens." Lastly, we provide the first patient-specific model calibration protocol that can estimate the remaining population dynamic and mechanical parameters based upon immunohistochemistry for proliferation (Ki-67, given as proliferative index), apoptosis (cleaved Caspase-3, given as apoptotic index), and various morphological measurements from hematoxylin and eosin (H&E) histopathology images *at a single time point*, allowing us to avoid the inherently inaccurate problem of estimating time derivatives from noisy patient data derived from a single sampling.

The organisation of this paper is as follows: In Section 1.1, we discuss the specific biology of normal breast epithelium and DCIS. After discussing relevant prior agent-based modelling (with a focus on DCIS) in Section 1.2, we introduce a composite agent-based cell model in Section 2 that builds upon and extends this reviewed work. In Section 3, we analyse the volume-averaged behaviour of the model in non-hypoxic regions. We close Part I by applying our volume-averaged analysis to individual breast ducts to formulate and test quantitative hypotheses on the relationships between oxygen, proliferation, and cell signalling heterogeneity in actual immunohistochemistry data (Section 4). We detail our interaction potential functions in Appendix A.

In Part II (Macklin et al., 2011), we apply our model to DCIS, introduce and test a patient-specific model calibration protocol based upon immunohistochemistry and histopathology, describe our numerical algorithms, simulate and analyse long-time DCIS growth in an individual, anonymised patient, and generate predictions on the rate of DCIS growth, the microstructure of the viable rim and necrotic core, and the relationship between the size of a tumour on a mammogram at the time of diagnosis (measured as a microcalcification) and its true morphological size, as measured by a pathologist post-operatively. These results are all tested against patient pathology and clinical data.

## 1.1   Ductal carcinoma in situ (DCIS) of the breast

Patient-specific DCIS simulation both motivates our model development and serves as a test bed for the resulting framework. We now discuss the specific biology of normal breast tissue and how that biology is subverted in DCIS.

5

For further pertinent biological background (including support for some modelling assumptions), see Macklin (2010) and the references therein. The biology discussed below is generally applicable to most epithelial malignancies.

### 1.1.1  Biology of breast duct epithelium

The breast is organised as a system of 12-15 independent, largely parallel duct systems: clusters of milk-producing lobules that feed into a branched duct system that terminates at the nipple (Wellings et al., 1975; Moffat and Going, 1996; Ohtake et al., 2001; Going and Mohun, 2006). The duct systems are separated by supporting ligaments and fatty tissue and drained by the lymphatic system (Tannis et al., 2001). Each duct is a tubular arrangement of epithelial cells that enclose a fluid-filled lumen. The epithelium, in turn, is surrounded by myoepithelial cells (epithelial cells with contractile properties to transport milk) and a basement membrane. Surrounding the duct is the stroma, which is comprised primarily of a supporting scaffolding of fibres (the extracellular matrix, or ECM) and mesenchymal cells that maintain the ECM. The stroma is interlaced by blood vessels that supply oxygen and other vital substrates to the tissue. See Fig. 1 (top left). Note that the breast epithelium has no direct access to oxygen and nutrients; these must diffuse into the duct through the BM.
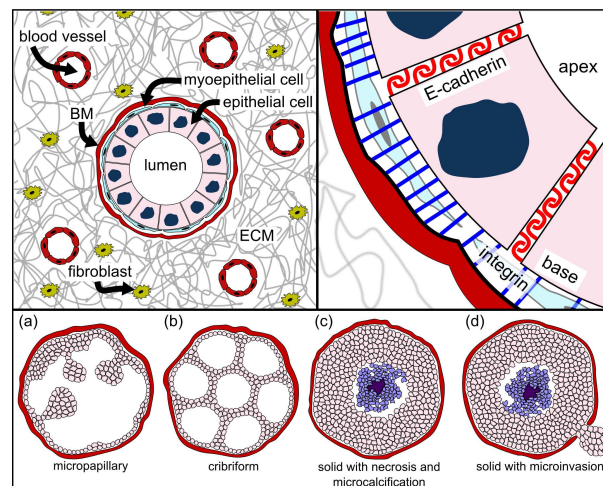


Fig. 1. *Top Left:* Typical breast duct microanatomy. *Top Right:* Breast duct epithelial cell polarisation. *Bottom:* Major DCIS types and invasive ductal carcinoma.

The epithelial cells are *polarised*: integrins on a well-defined basal side adhere to the basement membrane, E-cadherin molecules on the lateral sides adhere to neighbouring cells, and the apical side has relatively few adhesion molecules. See Fig. 1 (top right). The epithelial cell arrangement in the duct depends critically upon this polarisation and the resulting nonuniform distribution of adhesive forces (Jiang and Chuong, 1992; Hansen and Bissell, 2000; Wei et al., 2007; Butler et al., 2008).

While the epithelial cell population oscillates with the menstrual cycle (Khan et al., 1998, 1999), on average proliferation and apoptosis balance to maintain homeostasis. Microenvironmental changes can trigger signalling responses that lead to proliferation or apoptosis, which ordinarily helps to safeguard the normal tissue architecture. For example, a decrease of E-cadherin signalling (following apoptosis in a neighbouring cell) can increase $\beta$-catenin signalling, which eventually increases proliferation to replace the missing cell (Conacci-Sorrell et al., 2002; Hansen and Bissell, 2000; Wei et al., 2007). Adhesion to the BM triggers integrin signalling and downstream production of survival proteins that inhibit apoptosis (Ilić et al., 1998; Giancotti and Ruoslahti, 1999; Stupack and Cheresh, 2002). Loss of attachment to the BM therefore allows one type of apoptosis (*anoikis*) to occur, thus preventing overgrowth of cells into the lumen (Danes et al., 2008). Hormones such as estrogen, progesterone, prolactin, and epidermal growth factor can affect epithelial cell proliferation and apoptosis prior to lactation (Anderson, 2004), during breast involution (Baxter et al., 2007), and in cancer (Simpson et al., 2005).

*1.1.2   Biology of DCIS*

Overexpressed oncogenes and underexpressed tumour suppressor genes can disrupt the balance of epithelial cell proliferation and apoptosis, leading to overproliferation. This can occur typically either by the accumulation of DNA mutations (genetic damage) or DNA amplification (Simpson et al., 2005), or epigenetic anomalies (Ai et al., 2006). The transformation from regular breast epithelium to carcinoma is thought to occur in stages. For simplicity, we set aside the relatively benign precursor transformations (e.g., atypical ductal hyperplasia) which have a low risk for subsequent invasive breast cancer (Page, 1992) and focus on DCIS.

In the most well-differentiated classes of DCIS, the epithelial cells maintain their polarity and anisotropic adhesion receptor distributions, resulting in partial recapitulation of the non-pathological duct structure within the lumen. These demonstrate either finger-like growths into the lumen (micropapillary: see Fig. 1 (bottom:a)), or arrangements of duct-like structures (cribriform: see Fig. 1 (bottom:b)) (Silverstein, 2000). The cells in solid type DCIS lack polarity and do not develop these microstructures. Instead, the cells proliferate until filling the entire lumen (Fig. 1 (bottom:c)) (Danes et al., 2008). The proliferating cells uptake oxygen and nutrients as they diffuse into the duct, causing substrate gradients to form. If the central oxygen level is sufficiently depleted, a necrotic core of debris forms (comedo-type solid DCIS: see Fig. 1 (bottom:c)) (Silverstein, 2000). These necrotic cells are typically not phagocytosed; instead, they swell and burst (Barros et al., 2001), and their solid (i.e., non-water) components are slowly calcified (Stomper and Margolin, 1994). It is these calcifications that are generally detected by mammograms when di-

agnosing DCIS (Ciatto et al., 1994). The BM blocks DCIS from invading the stroma, thereby impeding spread through the stroma, invasion into lymphovascular channels and hence metastasis. Further mutations can transform DCIS into invasive ductal carcinoma, whose cells move along the duct, secrete matrix metalloproteinases (MMPs) to degrade the BM and subsequently invade the stroma (Fig. 1 (bottom:d)). See Silver and Tavassoli (1998) and Adamovich and Simmons (2003).

While it is tempting to regard DCIS as a linear progression from regular epithelium to cribriform or micropapillary ("partially transformed") to solid type ("fully transformed"), the morphological and molecular pathway is currently an open question (Erbas et al., 2006; Rennstam and Hedenfalk, 2006). The excellent modelling and analysis by Sontag and Axelrod (2005) strongly refutes a linear progression model. The dominant type of DCIS in any particular case may depend upon the underlying molecular changes. For example, cribriform DCIS could arise from hyperproliferative cells where genes regulating polarisation are functionally intact.

## 1.2  A sampling of prior agent-based cell modelling

It is beyond the scope of this paper to review all discrete biomathematics modelling; instead, we briefly review relevant prior agent-based models. For a broader and deeper review of discrete modelling, please see Lowengrub et al. (2010) and Macklin et al. (2010b) and the references therein.

While cellular automata methods are efficient for linking molecular- and cellular-scale biology in large numbers of virtual cells, they cannot accurately model cell and tissue mechanics due to the limitations they place upon cell arrangement (must be grid-aligned), size (all cells have equal size), velocity (cells move one cell diameter per time step), and interactions (can only interact with up to 8 neighbours in 2D). In particular, proliferation is disallowed in cells that are surrounded by cells in the adjacent computational mesh points; in actual tissue, interior cells can proliferate by deforming and pushing neighbouring cells into non-lattice configurations. In this paper, we use agent-based modelling (ABM), which eliminates the computational lattice and instead assigns each cell a position that evolves under the influence of forces acting upon it. Note that ABMs are sometimes referred to as individual-based models or particle methods. Alternative approaches include the lattice-gas method (Dormann and Deutsch, 2002), off-lattice cellular automata methods such as Voronoi-Delaunay models (Schaller and Meyer-Hermann, 2005), the immersed boundary cell model (Rejniak, 2007; Rejniak and Dillon, 2007; Rejniak and Anderson, 2008a,b), and the cellular potts technique (a.k.a. Graner-Glazier-Hogeweg model) (Graner and Glazier, 1992; Glazier and Garner, 1993).

An excellent agent-based model was developed by Drasdo, Höhme and co-workers (Drasdo et al., 1995; Drasdo and Höhme, 2003, 2005; Drasdo, 2005). Cells are modelled as roughly spherical, slightly compressible, and capable of migration, growth and division. Cell adhesion and repulsion (from limitations on cell deformation and compressibility) are modelled by introducing an inter-action energy; cells respond to proliferation and apoptosis in their neighbours by moving to reduce the total interaction energy using a stochastic algorithm. Ramis-Conde et al. (2008a,b) used a similar agent model, but instead used in-teraction potential functions to simulate cell-cell mechanics: cells move down the gradient of the potential, analogous to minimizing the interaction energy. Their work included a basic accounting for the cell-cell surface contact area, and related the strength of cell-cell adhesion to the concentration of E-cadherin/$\beta$-catenin complexes in the contact regions. Others have modelled cells as deformable viscoelastic ellipsoids (e.g., Dallon and Othmer (2004)).

Drasdo et al. (1995) initially developed their agent model to study epithelial cell-fibroblast-fibrocyte aggregations in connective tissue. More recently, they applied it to avascular tumour growth (Drasdo and Höhme, 2003), with bio-physical and kinetic parameters drawn from experimental literature (Drasdo and Höhme, 2005). More recently, Byrne and Drasdo (2009) upscaled a dis-crete model to calibrate a continuum tumour growth model, in part by us-ing a cell velocity-based approximation of the proliferative pressure to cal-ibrate the continuum-scale mechanics. Drasdo and co-workers were able to mechanistically model biomechanical growth limitations and the epithelial-to-mesenchymal transition in tumour cells, and they made testable hypotheses on the links between tumour hypoglycemia and the size of the necrotic core. Galle et al. (2005, 2009) extended the approach to include cell-BM adhesion, and its impact on cell differentiation and tumour monolayer progression. Ramis-Conde et al. (2008a,b) used their model to investigate the links between a sophisticated subcellular model of E-cadherin/$\beta$-catenin signalling, intercellu-lar signalling, and tissue morphology.

The very recent agent model of Norton et al. (2010) represented cell-cell ad-hesion and repulsion using a linear damped spring model, incorporated both apoptosis and necrosis, duct wall adhesion (through adhesion to myoepithelial cells), asymmetric progenitor cell division, and a simplified model of intraduc-tal fluid pressure. The model recapitulated solid-type, comedo-type, micropap-illary, and cribriform DCIS, illustrating the great potential in an agent-based modelling approach. However, the model lacked substrate transport, necro-sis was modelled by imposing the viable rim thickness *a priori* rather than through a combination of cell energetics and transport limitations, and pro-liferating cells were randomly distributed across the viable rim with uniform distribution; this contradicts immunohistochemical observations of the distri-bution of proliferating DCIS cells within the duct (e.g., as in Fig. 7). The authors did not treat necrotic core mechanics, which has a great impact on

9

the overall tumour morphology and rate of tumour advance in the duct. (See Part II (Macklin et al., 2011).) The observed microstructures were only partly mechanistic because the model enforced polarised cell-cell adhesion and "microlumens" algorithmically; in a mechanistic model, the tumour microstructure should not be imposed, but rather emerge naturally from the model's biophysics and population dynamics.

## 2 Agent-Based Cell Model

We now fully elaborate a discrete, cell-scale modelling framework that we first introduced in Macklin et al. (2009a, 2010b), which combines and extends some of the major features described in the models reviewed in Section 1.2. Our objective is a model that is sufficiently mechanistic that cellular and multicellular behaviour manifest themselves as *emergent phenomena* of the model, rather than through computational rules that are imposed *a priori*. We employ a modular design (in software and mathematics) that allows "sub-models" (e.g., molecular signalling, cell morphology) to be expanded, simplified, or outright replaced as necessary. Where possible, we choose simple sub-models and test the model framework's success in recapitulating correct DCIS behaviour.

Cells are modelled as physical objects that exchange forces; essential molecular biology is incorporated through carefully-chosen constitutive relations. We attempt to model the mechanics, time duration, and biology of each phenotypic state as accurately as our data will allow; this should facilitate calibration to molecular- and cellular data. The agents interact with the microenvironment through coupled partial differential equations governing substrate transport. We use the same model for both cancerous and non-cancerous cells. Functionally, the cells differ primarily in the values of their proliferation, apoptosis, and other parameters; this is analogous to the downstream effects of altered oncogenes and tumour suppressor genes (Hanahan and Weinberg, 2000).

In this discussion, cells are not polarised. We do not currently focus on stem cell dynamics; this can readily be added by identifying agents as stem cells, progenitor cells, or differentiated cells, and assigning each class different phenotypic characteristics. Thus, we focus on the growth and dynamics of DCIS, rather than its initiation. We do not explicitly model cell morphology, but rather total, nuclear, and solid volume. Where cell morphology is necessary, we approximate it as spherical, similarly to Ramis-Conde et al. (2008a,b). This approximation is further discussed in Section 2.1. Basement membranes are modelled using level set functions (Section 2.2), which can be adapted to model BM deformation (as discussed in Macklin et al. (2010b)).

## 2.1 Physical characteristics and mechanics

We endow each cell with a position $\mathbf{x}$, velocity $\mathbf{v}$, total volume $V$, solid volume $V_{\mathrm{S}}$, and nuclear volume $V_N$. We assume that $\mathbf{x}$ and $\mathbf{v}$ are at the cell's centre of mass and volume. While we do not explicitly track the cell morphology, we track the equivalent cell and nuclear radii (respectively $R$ and $R_{\mathrm{N}}$) via

$$V = \frac{4}{3}\pi R^3, \qquad V_N = \frac{4}{3}\pi R_{\mathrm{N}}^3. \tag{1}$$

See Fig. 2:left. For simplicity, we assume that $V_N$ is fixed throughout the cell cycle, and the solid volume maintains a constant percentage $V_{\mathrm{S}}/V$ of the total cell volume until entering the necrotic state. (See Section 2.5.4.)

Each cell has a maximum adhesion interaction distance $R_{\mathrm{A}} \geq R$, which we use to express several effects. Because cells are deformable, they can stretch beyond $R$ to maintain or create adhesive bonds. As we do not explicitly track the cell morphology, there is inherent uncertainty as to maximum extent of the cell boundary relative to its centre of mass; $R_{\mathrm{A}}$ needs to be sufficiently large to account for this. This effect is increased by random actin polymerisation/depolymerisation dynamics, which serve to randomly perturb the cell boundary (Gov and Gopinathan, 2006). See Fig. 2:right.

The cells are allowed to partly overlap to account for cell deformation. (Fig. 2: right.) We model the relative rigidity of the nucleus (relative to the cytoplasm) by introducing increased mechanical resistance to compression at a distances less than $R_{\mathrm{N}}$ from the cell centre; see Section 2.3.5 and Appendix A. Note that as $R_{\mathrm{N}} \uparrow R$ (most of the cell resists compression) or $R_{\mathrm{A}} \downarrow R$ (cells cannot deform to maintain adhesive contact), the cells behave like a granular material.

## 2.2 Basement membrane morphology

Let us denote the intraductal space (including both the epithelium and the lumen) by $\Omega$ and the basement membrane by $\partial\Omega$. We represent $\partial\Omega$ implicitly with an auxilliary signed distance function $d$ (a *level set function*) satisfying

$$\begin{cases} d(\mathbf{x}) > 0 & \mathbf{x} \in \Omega \\ d(\mathbf{x}) = 0 & \mathbf{x} \in \partial\Omega \\ d(\mathbf{x}) < 0 & \mathbf{x} \notin \overline{\Omega} = \Omega \cup \partial\Omega. \end{cases} \tag{2}$$

Additionally, $|\nabla d| \equiv 1$. See Fig. 3.

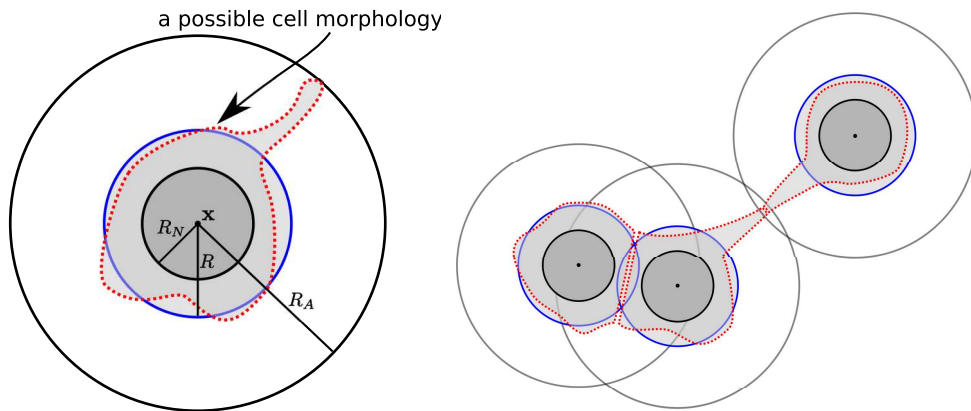This formulation can describe arbitrary BM geometries such as branch points

Fig. 2. **Cell morphology and mechanics:** _Left:_ We track the cell volume $V$ and nuclear volume $V_N$ (with equivalent spherical radii $R$ and $R_{\mathrm{N}}$), and solid volume $V_{\mathrm{S}}$. $R_{\mathrm{A}}$ is the maximum adhesive interaction distance. _Right:_ We account for uncertainty in the cell morphology by allowing the equivalent radii to overlap (left two cells), and by allowing adhesive contact beyond their equivalent radii (right two cells).
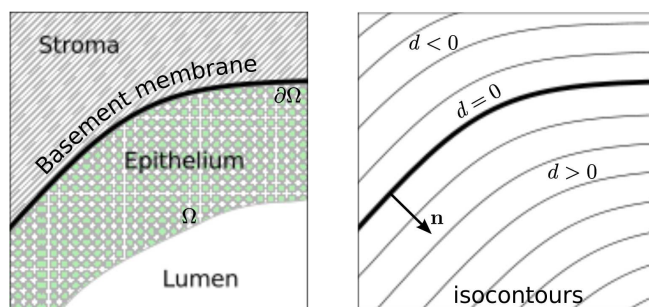


Fig. 3. **BM morphology:** _Left:_ The BM separates the epithelium and lumen from the stroma. _Right:_ The signed distance function $d$ represents the BM implicitly as its zero isocontour. $d > 0$ on the epithelial side, and $d < 0$ on the stromal side.

in breast duct tree structures. The normal vector $\mathbf{n}$ to the BM surface (oriented into the epithelium) is given by $\mathbf{n} = \nabla d$, and $\nabla \cdot \mathbf{n}$ gives the mean geometric curvature of the BM. This implicit representation is well-suited to describing a moving BM as it is deformed by mechanical stresses (e.g., due to proliferating tumour cells, as in Ribba et al. (2006)). See Macklin and Lowengrub (2005, 2006, 2007, 2008); Frieboes et al. (2007) and Macklin et al. (2009b), where we used this method to describe moving tumour boundaries.

## 2.3 Forces acting upon the cells

Each cell is subject to competing forces that determine its motion. Cells adhere to other cells (cell-cell adhesion: $\mathbf{F}_{\mathrm{cca}}$), the extracellular matrix (cell-ECM adhesion: $\mathbf{F}_{\mathrm{cma}}$), and the basement membrane (cell-BM adhesion: $\mathbf{F}_{\mathrm{cba}}$), calcified debris adheres to other calcified debris (debris-debris adhesion: $\mathbf{F}_{\mathrm{dda}}$),

cells and calcified debris resist compression by other cells and debris (cell-cell repulsion: $\mathbf{F}_{\mathrm{ccr}}$), and the basement membrane resists its penetration and deformation by cells and debris (cell-BM repulsion: $\mathbf{F}_{\mathrm{cbr}}$). Motile cells experience a net locomotive force $\mathbf{F}_{\mathrm{loc}}$ along the direction of intended travel. In addition, moving cells and debris experience a drag force $\mathbf{F}_{\mathrm{drag}}$ by the luminal and interstitial fluids, which we model by $\mathbf{F}_{\mathrm{drag}} = -\nu \mathbf{v}_i$. See Fig. 4. We currently neglect the impact of interstitial fluid pressure; this is equivalent to assuming the free flow of water, similarly to current continuum-scale mixture models (e.g., as in Wise et al. (2008); Bearer et al. (2009)). We express the balance of forces acting on cell $i$ by Newton's second law:

$$m_i \dot{\mathbf{v}}_i = \sum_{\substack{j=1 \\ j \neq i}}^{N(t)} \left( \mathbf{F}_{\mathrm{cca}}^{ij} + \mathbf{F}_{\mathrm{ccr}}^{ij} + \mathbf{F}_{\mathrm{dda}}^{ij} \right) + \mathbf{F}_{\mathrm{cma}}^{i} + \mathbf{F}_{\mathrm{cba}}^{i} + \mathbf{F}_{\mathrm{cbr}}^{i} + \mathbf{F}_{\mathrm{loc}}^{i} + \mathbf{F}_{\mathrm{drag}}^{i}. \quad (3)$$

Here, $N(t)$ is the number of cells in the simulation at time $t$. In this work, we focus on the impact of adhesive and repulsive forces, and set $\mathbf{F}_{\mathrm{loc}} = \mathbf{0}$
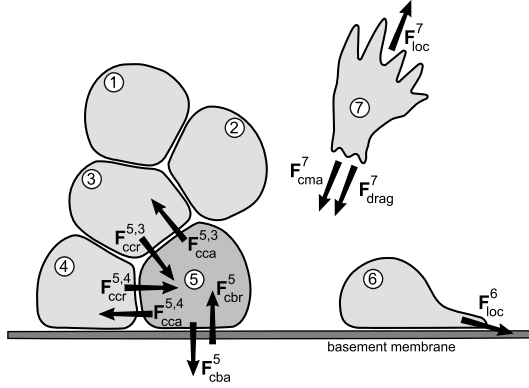


Fig. 4. **Agent model forces:** On Cell 5, find labelled the cell-cell adhesive ($\mathbf{F}_{\mathrm{cca}}^{5j}$) and repulsive ($\mathbf{F}_{\mathrm{ccr}}^{5j}$) forces, and the cell-BM adhesive ($\mathbf{F}_{\mathrm{cba}}^{5}$) and repulsive ($\mathbf{F}_{\mathrm{cbr}}^{5}$) forces. We label the net cell locomative force $\mathbf{F}_{\mathrm{loc}}^{i}$ for Cell 6 (undergoing motility along the BM) and Cell 7 (undergoing motility within the ECM). We show the cell-ECM adhesive force ($\mathbf{F}_{\mathrm{cma}}^{7}$) and fluid drag ($\mathbf{F}_{\mathrm{drag}}^{7}$) for Cell 7.

### 2.3.1 Cell-cell adhesion ($\mathbf{F}_{cca}$):

Adhesion molecules on a cell's surface bond with adhesive ligands (target molecules) on nearby cells. Hence, the strength of the adhesive force between the cells is (to first order) proportional to the product of the receptor and ligand expressions. The adhesion strength increases as the cells are drawn more closely together, bringing more surface area (and receptor-ligand pairs) into direct contact. We model the force imparted by cell $j$ on cell $i$ by

$$\mathbf{F}_{\mathrm{cca}}^{ij} = -\alpha_{\mathrm{cca}} f_{i,j} \nabla \varphi \left( \mathbf{x}_j - \mathbf{x}_i; R_{\mathrm{cca}}^{i} + R_{\mathrm{cca}}^{j}, n_{\mathrm{cca}} \right), \quad (4)$$

13

where $f_{i,j}$ describes the specific molecular biology of the adhesion, $R^i_{\mathrm{cca}}$ is cell $i$'s maximum adhesion interaction distance, and $\alpha_{\mathrm{cca}}$ is constant. The adhesive potential function $\varphi$ and the parameter $n_{\mathrm{cca}}$ are detailed in Appendix A.

**Homophilic adhesion:**   In homophilic adhesion (e.g., Panorchan et al. (2006)), adhesion receptors $\mathcal{E}$ bond with identical ligands $\mathcal{E}$. Hence,

$$f_{i,j} = \mathcal{E}_i \mathcal{E}_j, \tag{5}$$

where $\mathcal{E}_i$ is cell $i$'s (nondimensionalised) $\mathcal{E}$ receptor expression.

**Heterophilic adhesion:**   In heterophilic cell-cell adhesion (e.g, Springer (1990); Terol et al. (2003); Lucio et al. (1998)), adhesion receptors $\mathcal{I}_{\mathrm{A}}$ bond with dissimilar ligands $\mathcal{I}_{\mathrm{B}}$, and vice versa. Hence,

$$f_{i,j} = \mathcal{I}_{\mathrm{A},i}\mathcal{I}_{\mathrm{B},j} + \mathcal{I}_{\mathrm{B},i}\mathcal{I}_{\mathrm{A},j}, \tag{6}$$

where $\mathcal{I}_{\mathrm{A},i}$ and $\mathcal{I}_{\mathrm{B},i}$ are cell $i$'s (nondimensionalised) $\mathcal{I}_{\mathrm{A}}$ and $\mathcal{I}_{\mathrm{B}}$ expressions.

### 2.3.2   Cell-ECM adhesion ($\mathbf{F}_{cma}$):

Integrins $\mathcal{I}_{\mathrm{E}}$ on the cell surface form heterophilic bonds with suitable ligands $\mathcal{L}_{\mathrm{E}}$ in the ECM. We assume that $\mathcal{L}_{\mathrm{E}}$ is distributed proportionally to the (nondimensional) ECM density $E$. If $\mathcal{I}_{\mathrm{E}}$ is distributed uniformly across the cell surface and $E$ varies slowly relative to the spatial size of a single cell, then cells at rest encounter a uniform pull from $\mathbf{F}_{\mathrm{cma}}$ in all directions, resulting in zero net cell-ECM force. For cells in motion, $\mathbf{F}_{\mathrm{cma}}$ resists that motion similarly to drag due to the energy required to overcome $\mathcal{I} - \mathcal{L}$ bonds:

$$\mathbf{F}_{\mathrm{cma}} = -\alpha_{\mathrm{cma}}\mathcal{I}_{\mathrm{E},i}E\mathbf{v}_i. \tag{7}$$

Here, $\alpha_{\mathrm{cma}}$ is a constant. If $E$ or $\mathcal{L}_{\mathrm{E}}$ varies with a higher spatial frequency, or if $\mathcal{I}_{\mathrm{E}}$ is not uniformly distributed, then the finite half-life of $\mathcal{I}_{\mathrm{E}} - \mathcal{L}_{\mathrm{E}}$ bonds will lead to net haptotactic-type migration up gradients of $E$ (Macklin et al., 2010b). We model this effect as part of the net locomotive force $\mathbf{F}_{\mathrm{loc}}$.

### 2.3.3   Cell-BM adhesion ($\mathbf{F}_{cba}$):

Integrin molecules on the cell surface form heterophilic bonds with specific ligands $\mathcal{L}_{\mathrm{B}}$ (generally laminin and fibronectin (Butler et al., 2008)) on the basement membrane (with density $0 < B < 1$). We assume that $\mathcal{L}_{\mathrm{B}}$ is distributed proportionally to the (nondimensional) BM density $B$. Hence, the

strength of the cell-BM adhesive force is proportional to its integrin surface receptor expression and $B$. Furthermore, the strength of the adhesion increases as the cell approaches the BM, bringing more cell adhesion receptors in contact with their ligands on the BM. We model this adhesive force on cell $i$ by

$$\mathbf{F}^i_{\text{cba}} = -\alpha_{\text{cba}} \mathcal{I}_{\text{B},i} B \nabla \varphi \left( d(\mathbf{x}_i) \mathbf{n} \left( \mathbf{x}_i \right) ; R^i_{\text{cba}}, n_{\text{cba}} \right), \tag{8}$$

where $\alpha_{\text{cba}}$ is a constant, $d$ is the distance to the basement membrane, $\mathbf{n}$ is normal to the basement membrane (oriented towards the epithelial side of the membrane; see Section 2.2), $n_{\text{cba}}$ is as described in Appendix A, and $\mathcal{I}_{\text{B},i}$ and $R^i_{\text{cba}}$ are cell $i$'s (nondimensionalised) integrin receptor expression and maximum cell-BM adhesion interaction distance, respectively.

### 2.3.4 (Calcified) debris-(calcified) debris adhesion ($\mathbf{F}_{dda}$):

We model adhesion between calcified debris particles similarly to homophilic cell-cell adhesion: calcite crystals in the interacting calcified debris particles remain strongly bonded as part of the microcalcification. We model this cohesive force between the calcified debris particles $i$ and $j$ by

$$\mathbf{F}^{ij}_{\text{dda}} = -\alpha_{\text{dda}} C_i C_j \nabla \varphi \left( \mathbf{x}_j - \mathbf{x}_i; R^i_{\text{dda}} + R^j_{\text{dda}}, n_{\text{dda}} \right), \tag{9}$$

where $\alpha_{\text{dda}}$ is a constant, $C_i$ and $R^i_{\text{dda}}$ are cell $i$'s (nondimensionalised) degree of calcification and maximum debris-debris adhesion interaction distance, and $n_{\text{dda}}$ is the exponent described in Appendix A.

### 2.3.5 Cell-cell repulsion (including calcified debris) ($\mathbf{F}_{ccr}$):

Cells resist compression by other cells due to the structure of their cytoskeletons, the incompressibility of their cytoplasm, and the surface tension of their membranes. We introduce a cell-cell repulsive force that is zero when cells are just touching, and increases rapidly as the cells are pressed together, particularly when their nuclei are in close proximity. We approximate cell deformation by allowing partial cell overlap. See Section 2.1. We model $\mathbf{F}_{\text{ccr}}$ by

$$\mathbf{F}^{ij}_{\text{ccr}} = -\alpha_{\text{ccr}} \nabla \psi \left( \mathbf{x}_j - \mathbf{x}_i; R^i_{\text{N}} + R^j_{\text{N}}, R_i + R_j, M, n_{\text{ccr}} \right), \tag{10}$$

where $\alpha_{\text{ccr}}$ is a constant, $R^i_{\text{N}}$ and $R_i$ are cell $i$'s nuclear radius and radius, respectively, and $M$ and $n_{\text{ccr}}$ are described in Appendix A.

### 2.3.6 Cell-BM repulsion (including debris) ($\mathbf{F}_{cbr}$):

We model the basement membrane as rigid and thus resistant to deformation and penetration by the cells and debris. We model this force by

$$\mathbf{F}^i_{\text{cbr}} = -\alpha_{\text{cbr}} B \nabla \psi \left( d(\mathbf{x}_i) \mathbf{n}\left(\mathbf{x}_i\right); R^i_{\text{N}}, R_i, M, n_{\text{cbr}} \right), \qquad (11)$$

where $\alpha_{\text{cbr}}$ is a constant, $d$ is the distance to the BM, $R^i_{\text{N}}$ and $R_i$ are described earlier, and $M$ and $n_{\text{cbr}}$ are described in Appendix A. We discuss planned work to model viscoplastic membrane expansion in Macklin et al. (2010b).

### 2.4 "Inertialess" assumption; Relationship to continuum-scale Darcy's law

Similarly to Drasdo et al. (1995); Galle et al. (2005) and Ramis-Conde et al. (2008b) and as discussed in Lowengrub et al. (2010), we make the "inertialess" assumption that the forces equilibrate quickly, and so $|m_i \dot{\mathbf{v}}_i| \approx 0$. Hence, we approximate $\sum \mathbf{F} = \mathbf{0}$ and solve for the cell velocity from Eq. 3:

$$\mathbf{v}_i = \frac{1}{\nu + \alpha_{\text{cma}} \mathcal{I}_{\text{E},i} E} \left( \sum_{\substack{j=1 \\ j \neq i}}^{N(t)} \left( \mathbf{F}^{ij}_{\text{cca}} + \mathbf{F}^{ij}_{\text{dda}} + \mathbf{F}^{ij}_{\text{ccr}} \right) + \mathbf{F}^i_{\text{cba}} + \mathbf{F}^i_{\text{cbr}} + \mathbf{F}^i_{\text{loc}} \right). (12)$$

This has a convenient interpretation: each term $\frac{1}{\nu + \alpha_{\text{cma}} \mathcal{I}_{\text{E},i} E} \mathbf{F}_{\square}$ is the "terminal" (equilibrium) velocity of the cell when fluid drag, cell-ECM adhesion, and $\mathbf{F}_{\square}$ are the only forces acting upon it. Here, "$\square$" represents any individual force above, e.g., cba, cca, etc., and $N(t)$ is the number of simulated cells at time $t$.

It is interesting to compare Eq. 12 with Darcy's law, the basis of many continuum-scale tumour models such as Cristini et al. (2003); Macklin and Lowengrub (2005, 2006, 2007, 2008) and Macklin et al. (2009b). In these models, tumour growth is considered as incompressible flow in a porous medium (the ECM). A mechanical pressure $P$ is used to model tissue mechanics as a balance of proliferation-induced stresses, adhesion, and tissue relaxation. If $\mathbf{u}(\mathbf{x},t)$ is the mean tissue velocity at $\mathbf{x}$, then the Darcy's law formulation of the tissue mechanics is given by

$$\mathbf{u} = -\mu \nabla P. \qquad (13)$$

See the extensive review, discussion, and references in Lowengrub et al. (2010).

The *mobility* coefficient $\mu$ models the ability of cells to mechanically respond to pressure gradients by overcoming cell-cell and cell-ECM adhesive bonds, or by deforming the ECM (Macklin and Lowengrub, 2007). In Frieboes et al.

(2007) and Macklin et al. (2009b), we introduced a functional relationship between the mobility $\mu$ and the ECM density $E$ of the form

$$\mu = \frac{1}{\alpha + \beta E + \frac{1}{\epsilon}S}, \tag{14}$$

where $S$ is a "structure variable" that models the presence ($S = 1$) or absence ($S = 0$) of rigid barriers, $\epsilon \approx 0$, and $\alpha$ and $\beta$ are constants. When $S = 0$, Eq. 14 is identical to the coefficient in Eq. 12. While Eq. 14 was initially chosen as the simplest possible with biologically-reasonable qualitative behaviour (mobility decreases as the ECM density increases, rendering the tissue less "permeable" to cells), we now see it is fully consistent with the cell-scale biophysics presented above.

## 2.5  Cell States

We endow each agent with a phenotypic state $\mathcal{S}(t)$ in the state space $\{\mathcal{Q}, \mathcal{P}, \mathcal{A}, \mathcal{H}, \mathcal{N}, \mathcal{C}, \mathcal{M}\}$ (introduced below). Quiescent cells ($\mathcal{Q}$) are in a "resting state" ($G_0$, in terms of the cell cycle); this is the "default" state in the framework. We model the transitions between cell states as stochastic events governed by exponentially-distributed random variables that are linked to the cell's genetic and proteomic state, as well as the microenvironment. These exponentially-distributed variables can be regarded as arising from nonhomogeneous Poisson processes; the interested reader can find a brief discussion in the supplementary material.

For a transition to state $\mathcal{S}_2$ from the current state $\mathcal{S}_1$, and for any interval $(t, t + \Delta t]$, we use the general form

$$\Pr\left(\mathcal{S}(t + \Delta t) = \mathcal{S}_2 | \mathcal{S}(t) = \mathcal{S}_1\right) = 1 - \exp\left(-\int_t^{t+\Delta t} \alpha_{12}(\mathcal{S}, \bullet, \circ)(s)\, ds\right), \tag{15}$$

where $\alpha_{12}\left(\mathcal{S}, \bullet, \circ\right)(t)$ is the intensity function, $\bullet$ represents the cell's internal (genetic and proteomic) state, and $\circ$ represents the state of the surrounding microenvironment sampled at the cell's position $\mathbf{x}(t)$. Note that for small $\Delta t$,

$$\Pr\left(\mathcal{S}(t + \Delta t) = \mathcal{S}_2 | \mathcal{S}(t) = \mathcal{S}_1\right) = \alpha_{12}\left(\mathcal{S}, \bullet, \circ\right)(t)\Delta t + \mathcal{O}\left(\Delta t^2\right); \tag{16}$$

when $\alpha_{12}$ is constant, we recover (to second order) the commonly-used constant transition probabilites for fixed step sizes $\Delta t$; these may be regarded as approximations to our more general model here.

If $\mathcal{S}_1 \rightarrow \mathcal{S}_2$ transitions depend upon two separate processes with characteristic transition intensities $\alpha'_{12}$ and $\alpha^*_{12}$, we may choose $\alpha_{12} = \alpha'_{12} + \alpha^*_{12}$ when these
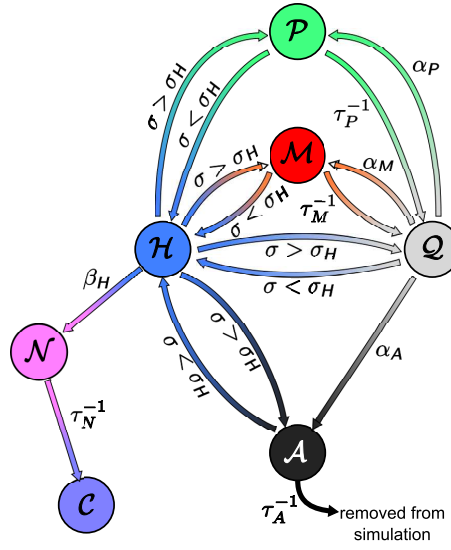
Fig. 5. Phenotypic transition network in the agent-based model.

processes are independent. In this case, for small $\Delta t$,

$$\Pr\left(\mathcal{S}(t+\Delta t) = \mathcal{S}_2 | \mathcal{S}(t) = \mathcal{S}_1\right) \approx \left(\alpha'_{12}\left(\mathcal{S}, \bullet, \circ\right)(t) + \alpha^*_{12}\left(\mathcal{S}, \bullet, \circ\right)(t)\right)\Delta t \quad (17)$$

which is approximately the probability of a $\mathcal{S}_1 \to \mathcal{S}_2$ transition due to either the $\alpha'_{12}$ process or the $\alpha^*_{12}$ process.

If the processes are not independent, we choose the form $\alpha_{12} = \alpha'_{12}\alpha^*_{12}$, yielding

$$\Pr\left(\mathcal{S}(t+\Delta t) = \mathcal{S}_2 | \mathcal{S}(t) = \mathcal{S}_1\right) \approx \left(\alpha'_{12}\left(\mathcal{S}, \bullet, \circ\right)(t) \cdot \alpha^*_{12}\left(\mathcal{S}, \bullet, \circ\right)(t)\right)\Delta t, \quad (18)$$

which is approximately the probabilty of both $\alpha'_{12}$ and $\alpha^*_{12}$ processes "allowing" an $\mathcal{S}_1 \to \mathcal{S}_2$ transition; $\alpha'_{12}$ and $\alpha^*_{12}$ are rate-limiting processes for one another.

In our cell phenotypic state space, quiescent cells can become proliferative ($\mathcal{P}$), apoptotic ($\mathcal{A}$), or motile ($\mathcal{M}$). (In the work below, we shall neglect the motile state.) Cells in any state can become hypoxic ($\mathcal{H}$); hypoxic cells can recover to their previous state or become necrotic ($\mathcal{N}$), and necrotic cells are degraded and gradually replaced by (clinically-detectable) calcified debris ($\mathcal{C}$). See Fig. 5. The subcellular scale is built into this framework by making the random exponential variables depend upon the microenvironment and the cell's internal properties.

Note that cell cycle models have also been developed to regulate the $\mathcal{P} \to \mathcal{Q}$ transition (e.g., Abbott et al. (2006) and Zhang et al. (2007)), and signalling networks have been developed to regulate the $\mathcal{Q} \to \{\mathcal{P}, \mathcal{A}, \mathcal{M}\}$ transitions. These can be directly integrated into the agent framework presented here by modifying the stochastic parameters or by outright replacing the exponential random variables with deterministic processes (Macklin et al., 2010b). Some

18

excellent examples of agent-based modelling with subcellular signalling components include Chen et al. (2009b,a); Kharait et al. (2007); Wang et al. (2007) and Zhang et al. (2007, 2009).

### 2.5.1  Proliferation ($\mathcal{P}$):

As suggested by experimental and theoretical work as early as Smith and Martin (1973), quiescent cells enter the proliferative state (i.e., progress from $G_0$ to S) with a probability that depends upon the microenvironment. We model the probability of a quiescent cell entering the proliferative state in the time interval $(t, t + \Delta t]$ via an exponential random variable:

$$\Pr\left(\mathcal{S}(t + \Delta t) = \mathcal{P}|\mathcal{S}(t) = \mathcal{Q}\right) = 1 - \exp\left(- \int_t^{t+\Delta t} \alpha_{\mathrm{P}}(\mathcal{S}, \bullet, \circ)(s) \, ds\right)$$

$$\approx 1 - \exp\left(-\alpha_{\mathrm{P}}(\mathcal{S}, \bullet, \circ)(t)\Delta t\right), \qquad (19)$$

where the approximation best holds when $\alpha_{\mathrm{P}}$ varies slowly relative to $\Delta t$.

Assuming a correlation between the microenvironmental oxygen level $\sigma$ (non-dimensionalised by the far-field oxygen level in non-diseased, normoxic tissue) and proliferation (See Section 4, as well as the excellent discussion and references in Silva and Gatenby (2010)), we expect $\alpha_{\mathrm{P}}$ to increase with $\sigma$. Hence:

$$\alpha_{\mathrm{P}} = \alpha_{\mathrm{P}}(\mathcal{S}, \sigma, \bullet, \circ)(t) = \begin{cases} \overline{\alpha}_{\mathrm{P}}(\bullet, \circ)\frac{\sigma - \sigma_{\mathrm{H}}}{1 - \sigma_{\mathrm{H}}} & \text{if } \mathcal{S}(t) = \mathcal{Q} \\ 0 & \text{else,} \end{cases} \qquad (20)$$

where $\sigma_{\mathrm{H}}$ is a threshold oxygen value at which cells become hypoxic, and $\overline{\alpha}_{\mathrm{P}}(\bullet, \circ)$ is the cell's $\mathcal{Q} \to \mathcal{P}$ transition rate when $\sigma = 1$ (i.e., in normoxic, non-pathologic tissue), which depends upon the cell's genetic profile and protein signalling state ($\bullet$) and the local microenvironment ($\circ$). Note that in tumours, low oxygenation is the norm (Gatenby et al., 2007; Smallbone et al., 2007), and so $\sigma$ is far below 1. In Part II, we generally find that $\sigma_H \sim 0.2$ and $\sigma < 0.4$.

For simplicity, we model $\overline{\alpha}_P$ as constant for and specific to each cell type. In Macklin et al. (2010b), we discuss how to incorporate $\bullet$ (i.e., a cell's internal protein expression) and $\circ$ (as sampled by a cell's surface receptors) into $\alpha_{\mathrm{P}}$ through a subcellular molecular signalling model. We note that models have been developed that reduce the proliferation rate in response to mechanical stresses (e.g., see the excellent description by Shraiman (2005)); in the context of the model, the cell samples these stresses from continuum-scale field variables or tensors (i.e., "$\circ$") to reduce $\alpha_{\mathrm{P}}$.

Once a cell has entered the proliferative state $\mathcal{P}$, it remains in that state until dividing into two identical daughter cells of half volume, which themselves

remain in $\mathcal{P}$ until "maturing" into full-sized cells at the end of $G_1$. Thereafter, the daughter cells are placed in the "default" quiescent state $\mathcal{Q}$ to simulate the transition from $G_1$ to $G_0$. We now describe these events in greater detail.

Define $\tau$ to the ellapsed time since the cell entered the cell cycle from $\mathcal{Q}$. Similarly to Ramis-Conde et al. (2008b), we divide the cell cycle (with duration $\tau_P$) into the S-M phases and the $G_1$ phase (with duration $\tau_{G1}$). While $\tau_P$ and $\tau_{G1}$ may generally depend upon the microenvironment and the cell's internal state, we currently model them as fixed for any given cell type.
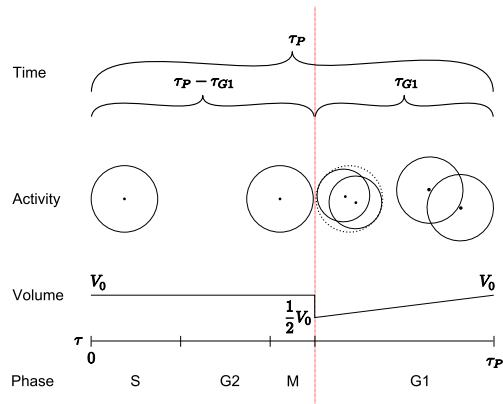


Fig. 6. $\mathcal{P}$ **submodel:** A cell enters $\mathcal{P}$ from the quiescent state $\mathcal{Q}$, modelling the $G_0$ to S transition. It then remains in $\mathcal{P}$ until dividing into two identical daughter cells of half volume. The daughter cells also remain in $\mathcal{P}$ until completing $G_1$ and "maturing" into full-sized cells; thereafter, they enter the "default" state $\mathcal{Q}$.

At time $\tau = \tau_P - \tau_{G1}$ (at the end of M), we divide the cell into two identical daughter cells with half the mass and volume of the parent cell. We assume that both daughter cells evenly inherit the parent cell's surface receptor expressions, internal protein expressions, and genetic characteristics (as embodied by the phenotypic state transition parameters). We position the daughter cells randomly, subject to two constraints:

(1) The daughter cells preserve the parent cell's centre of volume; and
(2) The daughter cells (when considered as spheres) are fully contained within the same volume as the former parent cell.

We accomplish this by placing the daughter cell centres symmetrically about the parent cell's centre, such that they fit within the parent cell's equivalent sphere. See Fig. 6. Thus, the cells partially overlap after mitosis; cell-cell repulsive forces (see Section 2.3.5) subsequently push them apart. This overlap partly accounts for the non-spherical cell geometry following mitosis.

20

We simulate a proliferating cell's changing volume $V$ by

$$V(\tau) = \begin{cases} V_0 & 0 \leq \tau \leq \tau_{\mathrm{P}} - \tau_{\mathrm{G1}} \\ \frac{1}{2}V_0 \left(1 + \frac{\tau_{\mathrm{G1}} + (\tau - \tau_{\mathrm{P}})}{\tau_{\mathrm{G1}}}\right) & \tau_{\mathrm{P}} - \tau_{\mathrm{G1}} \leq \tau \leq \tau_{\mathrm{P}}, \end{cases} \tag{21}$$

where $V_0$ is the cell's "mature" volume.

### 2.5.2 Apoptosis ($\mathcal{A}$):

Apoptotic cells undergo "programmed" cell death in response to signalling events. As with proliferation, we model entry into $\mathcal{A}$ using an exponentially-distributed random variable with parameter $\alpha_{\mathrm{A}}(t) = \alpha_{\mathrm{A}}(\mathcal{S}, \bullet, \circ)(t)$. We assume no correlation between apoptosis and oxygen (Edgerton et al., 2011):

$$\Pr\left(\mathcal{S}(t + \Delta t) = \mathcal{A} | \mathcal{S}(t) = \mathcal{Q}\right) = 1 - \exp\left(-\int_t^{t+\Delta t} \alpha_{\mathrm{A}}(s)\, ds\right)$$
$$\approx 1 - \exp\left(-\alpha_{\mathrm{A}}(t)\Delta t\right), \tag{22}$$

where

$$\alpha_{\mathrm{A}}(t) = \alpha_{\mathrm{A}}(\mathcal{S}, \bullet, \circ)(t) = \begin{cases} \overline{\alpha}_{\mathrm{A}}(\bullet, \circ) & \text{if } \mathcal{S}(t) = \mathcal{Q} \\ 0 & \text{else,} \end{cases} \tag{23}$$

and where $\circ$ does not include oxygen $\sigma$, but may include other microenvironmental stimuli such as proximity of the BM (anoikis), chemotherapy, or continuum-scale mechanical stresses that increase $\alpha_{\mathrm{A}}$ as in Shraiman (2005). Cells remain in the apoptotic state for a fixed amount of time $\tau_{\mathrm{A}}$; afterward they are removed from the simulation to model phagocytosis of apoptotic bodies. Their previously-occupied volume is made available to the surrounding cells to model the release of the cells' water content after lysis.

### 2.5.3 Hypoxia ($\mathcal{H}$):

Cells enter the hypoxic state at any time that $\sigma < \sigma_{\mathrm{H}}$. Hypoxic cells have an exposure time-dependent probability of becoming necrotic:

$$\Pr\left(\mathcal{S}(t + \Delta t) = \mathcal{N} | \mathcal{S}(t) = \mathcal{H}\right) = 1 - \exp\left(-\int_t^{t+\Delta t} \beta_{\mathrm{H}}(\sigma)(s)\, ds\right) ds$$
$$\approx 1 - \exp\left(-\beta_{\mathrm{H}}\left(\sigma\right)(t)\Delta t\right). \tag{24}$$

We currently model $\beta_{\mathrm{H}}(\sigma)(t)$ as constant, although it could readily be made dependent upon $\sigma$ to more explicitly model energy depletion, such as in Smallbone et al. (2007) and Silva and Gatenby (2010). If $\sigma > \sigma_{\mathrm{H}}$ (normoxia is

restored) at time $t + \Delta t$ and the cell has not become necrotic, it returns to its former state and resumes its activity. For example, if the cell transitioned from $\mathcal{P}$ to $\mathcal{H}$ after spending $\tau$ time in the cell cycle, and normoxic conditions are restored, then it returns to $\mathcal{P}$ with $\tau$ time having elapsed in its cell cycle progression. Notice that by Eq. 24, the probability that a cell succumbs to hypoxia increases with $\Delta t$ whenever $\mathcal{S} = \mathcal{H}$, independently of previous states. Hence, this probability scales (nonlinearly) with its cumulative exposure time to hypoxia. This construct could model cell response to other stressors (e.g., chemotherapy), similarly to "area under the curve" models (e.g., El-Kareh and Secomb (2003, 2005)).

### 2.5.4 Necrosis ($\mathcal{N}$):

In our model, a hypoxic cell has a probability of irreversibly entering the necrotic state, simulating depletion of its ATP store. We can also simplify the model and neglect the hypoxic state by letting $\beta_H \to \infty$.

We assume that a cell remains in $\mathcal{N}$ for a fixed amount of time $\tau_N$, during which time its surface receptors and subcellular structures degrade, it loses its liquid volume, and calcium is deposited (primarily) in its solid fraction. We define $\tau_{NL}$ to be the length of time for the cell to swell, lyse, and lose its water content, $\tau_{NS}$ the time for all surface receptors to degrade and become functionally inactive, and $\tau_C$, the time for calcification to occur. We assume that $\tau_{NL} \leq \tau_{NS} < \tau_C = \tau_N$. In Macklin et al. (2009a) we found that a simplified model (where $\tau_N = \tau_{NS} = \tau_{NL} = \tau_C$) could not reproduce certain morphological aspects of the viable rim-necrotic core interface in breast cancer.

If $\tau$ is the elapsed time spent in the necrotic state, we model the degradation of the surface receptor species $S$ (scaled by the non-necrotic expression level) by exponential decay with rate constant $\log 100/\tau_{NS}$; the constant is chosen so that $S(\tau_{NS}) = 0.01\, S(0)$, i.e., virtually all of the surface receptor is degraded by time $\tau = \tau_{NS}$. After time $\tau_{NS}$, we set $S = 0$.

To model the necrotic cell's volume change, let $f_{NS}$ be the maximum percentage increase in the cell's volume (just prior to lysis), and let $V_0$ be the cell's volume at the onset of necrosis. Then

$$V(\tau) = \begin{cases} V_0 \left(1 + f_{NS}\dfrac{\tau}{\tau_{NL}}\right) & \text{if } 0 \leq \tau < \tau_{NL} \\ V_S & \text{if } \tau_{NL} < \tau, \end{cases} \tag{25}$$

where $V_S$ is the cell's solid volume. If the cell's nuclear radius $R_N$ exceeds its equivalent radius $R$ after lysis, then we set $R_N = R$. To model uncertainty in the cell morphology during lysis, we randomly perturb its location $\mathbf{x}$ such that its new radius $R(\tau_{NL})$ is contained within its swelled radius $R(0)\,(1 + f_{NS})^{\frac{1}{3}}$.

Lastly, we assume a constant rate of cell calcification, with the necrotic cell reaching a clinically-detectable level of calcification at time $\tau_{\rm C}$. If $C$ is the nondimensional degree of calcification, then $C(t) = \tau/\tau_{\rm C}$.

### 2.5.5 Calcified debris ($\mathcal{C}$):

Necrotic cells are gradually calcified until reaching a clinically-detectable level of calcification; such cells make an irreversible $\mathcal{N} \to \mathcal{C}$ transition. Lacking functional adhesion receptors, these cells only adhere to other calcified debris; this is a simplified model of the crystalline bonds in the calcification.

## 2.6 Dynamic coupling with the microenvironment with upscaling

We integrate the agent model with the microenvironment as part of a discrete-continuum composite model, demonstrating here with a coupling to oxygen transport; further examples including ECM-MMP dynamics are given in Macklin et al. (2010b). We do this by introducing field variables for key microenvironmental components (e.g., oxygen, signalling molecules, extracellular matrix, etc.) that are updated according to continuum equations. The distributions of these variables affect the cell agents' evolution as already described; simultaneously, the agents impact the evolution of the continuum variables. In the language of Deisboeck et al. (2010), this is a *composite hybrid* model.

### 2.6.1 Oxygen transport

All cell agents uptake oxygen as a part of metabolism. At the macroscopic scale, this is modelled by

$$\frac{\partial \sigma}{\partial t} = \nabla \cdot (D\nabla\sigma) - \lambda\sigma, \tag{26}$$

where $\sigma$ is oxygen, $D$ is its diffusion constant, and $\lambda$ is the (spatiotemporally variable) uptake/decay rate. Suppose that viable (non-necrotic, non-calcified) tumour cells uptake oxygen at a rate $\lambda_{\rm t}$, host cells at a rate $\lambda_{\rm h}$, and elsewhere oxygen "decays" (by reacting with the molecular landscape) at a low background rate $\lambda_{\rm b}$. Suppose that in a small neighbourhood $B$ of $\mathbf{x}$, tumour cells, host cells, and stroma (non-cells) respectively occupy fractions $f_{\rm t}$, $f_{\rm h}$, and $f_{\rm b}$ of $B$, where $f_{\rm t} + f_{\rm h} + f_{\rm b} = 1$. Then $\lambda(\mathbf{x})$ is given by

$$\lambda(\mathbf{x}) \approx f_{\rm t}\lambda_{\rm t} + f_{\rm h}\lambda_{\rm h} + f_{\rm b}\lambda_{\rm b}, \tag{27}$$

i.e., by averaging the uptake rates with weighting according to the tissue composition near $\mathbf{x}$. This is consistent with the uptake rate model by Hoehme

and Drasdo (2010), which they based upon the experimental literature.

We could further decompose $f_t$ and $f_h$ according to cell phenotype, if the uptake rates were expected to vary. In numerical implementations, we generally compute $\lambda$ at a scale that resolves the cells (e.g., mesh size $\sim 1\,\mu\text{m}$) and then upscale it to the computational mesh. See Part II (Macklin et al., 2011). In this formulation, the cell uptake rate varies with the tumour microstructure, which, in turn, evolves according to nutrient and oxygen availability.

Boundary conditions vary by the biology of the modelled problem. In our work, we set $\sigma = \sigma_B$ (for a fixed boundary value $\sigma_B$ on the basement membrane and inside the stroma (wherever $d \leq 0$) to model the release of oxygen by a pre-existent vasculature in the stroma. Wherever the simulation boundary intersects lumen, we use Neumann boundary conditions.

## 3 Analysis of the volume-averaged model behaviour

Let us fix a volume $\Omega$ contained within a non-hypoxic, non-necrotic tissue (i.e., all cells $i$ in $\Omega$ satisfy $\mathcal{S}_i \notin \{\mathcal{H}, \mathcal{N}, \mathcal{C}\}$). We analyse the population dynamics in the simplified $\mathcal{Q}$-$\mathcal{A}$-$\mathcal{P}$ cell state network; this analysis is the basis of the model calibration in Part II (Macklin et al., 2011). Let $P(t)$, $A(t)$, and $Q(t)$ denote the number of proliferating, apoptosing, and quiescent cells in $\Omega$ at time $t$, respectively. Let $N(t) = P + A + Q$. If $\langle \alpha_P \rangle(t) = \frac{1}{|\Omega|} \int_\Omega \alpha_P \, dV$ is the mean value of $\alpha_P$ at time $t$ throughout $\Omega$, then the net number of cells entering state $\mathcal{P}$ in the time interval $[t, t + \Delta t)$ is approximately

$$P(t + \Delta t) = P(t) + \Pr\left(\mathcal{S}(t + \Delta t) = \mathcal{P}|\mathcal{S}(t) = \mathcal{Q}\right) Q(t) - \frac{1}{\tau_P} P(t)\Delta t$$

$$\approx P(t) + \left(1 - e^{-\langle \alpha_P \rangle \Delta t}\right) Q(t) - \frac{1}{\tau_P} P(t)\Delta t, \tag{28}$$

whose limit as $\Delta t \downarrow 0$ (after some rearrangement) is

$$\dot{P} = \langle \alpha_P \rangle Q - \frac{1}{\tau_P} P. \tag{29}$$

Similarly,

$$\dot{A} = \alpha_A Q - \frac{1}{\tau_A} A \tag{30}$$

$$\dot{Q} = 2\frac{1}{\tau_P} P - \left(\langle \alpha_P \rangle + \alpha_A\right) Q. \tag{31}$$

Summing these, we obtain

$$\dot{N} = \frac{1}{\tau_P} P - \frac{1}{\tau_A} A. \tag{32}$$

Next, define PI $= P/N$ and AI $= A/N$ to be the *proliferative* and *apoptotic indices*, respectively. We can express the equations above in terms of AI and PI by dividing by $N$ and using Eq. 32 to properly treat $\frac{d}{dt}(P/N)$ and $\frac{d}{dt}(A/N)$. After simplifying, we obtain a nonlinear system of ODEs for PI and AI:

$$\dot{PI} = \langle \alpha_P \rangle (1 - AI - PI) - \frac{1}{\tau_P} \left( PI + PI^2 \right) + \frac{1}{\tau_A} AI \cdot PI \tag{33}$$

$$\dot{AI} = \alpha_A (1 - AI - PI) - \frac{1}{\tau_A} \left( AI - AI^2 \right) - \frac{1}{\tau_P} AI \cdot PI. \tag{34}$$

These equations are far simpler to compare to immunohistochemical measurements, which are generally given in terms of AI and PI.

Lastly, let us nondimensionalise the equations by letting $t = \hat{t}\,\bar{t}$, where $\hat{t}$ is dimensionless. Then if $f' = \frac{d}{d\hat{t}} f$, we have

$$\frac{1}{\bar{t}} PI' = \langle \alpha_P \rangle (1 - AI - PI) - \frac{1}{\tau_P} \left( PI + PI^2 \right) + \frac{1}{\tau_A} AI \cdot PI \tag{35}$$

$$\frac{1}{\bar{t}} AI' = \alpha_A (1 - AI - PI) - \frac{1}{\tau_A} \left( AI - AI^2 \right) - \frac{1}{\tau_P} AI \cdot PI. \tag{36}$$

The cell cycle length $\tau_P$ is on the order of 1 day (e.g., as in Owen et al. (2004)), and in Part II (Macklin et al., 2011), we determine that $\tau_A$ is of similar magnitude. Thus, if we choose $\bar{t} \sim \mathcal{O}(10\text{ day})$ or greater, then we can assume that $\frac{1}{\bar{t}} PI' = 0 = \frac{1}{\bar{t}} AI'$ and conclude that the local cell state dynamics reach steady state after after 10-100 days. This is significant, because it allows us to calibrate the population dynamic parameters ($\alpha_A$, $\alpha_P$, $\tau_A$, and $\tau_P$) without the inherent difficulty of estimating time derivatives from often noisy *in vitro* and immunohistochemistry data. This result is consistent with our earlier mathematical analysis in Macklin and Lowengrub (2007), which hypothesised "local equilibriation" of the tumour microstructure, even during growth.

## 4   Volume-averaged model behaviour, and testable hypotheses

We conclude Part I by applying a volume-averaged analysis to the viable rim in DCIS to generate biological hypotheses that we test against immunohistochemistry data. For fixed AI, PI, $\tau_A$, and $\tau_P$, we can use Eqs. 33-34 to

determine $\langle \alpha_{\mathrm{P}} \rangle$ and $\alpha_{\mathrm{A}}$, and ultimately, $\overline{\alpha}_P$; see Part II for full details (Macklin et al., 2011). In Macklin et al. (2009a), we instead treated $\alpha_{\mathrm{A}}$ and $\overline{\alpha}_P$ and constant and solved the nonlinear ODE system for PI and AI to steady state as a function of $0 \leq \sigma \leq 1$. This analysis led us to predict Michaelis-Menten population kinetics as an emergent model phenomenon: for sufficient oxygen availability, proliferation saturates, indicating that oxygenation is no longer the primary growth-limiting factor.
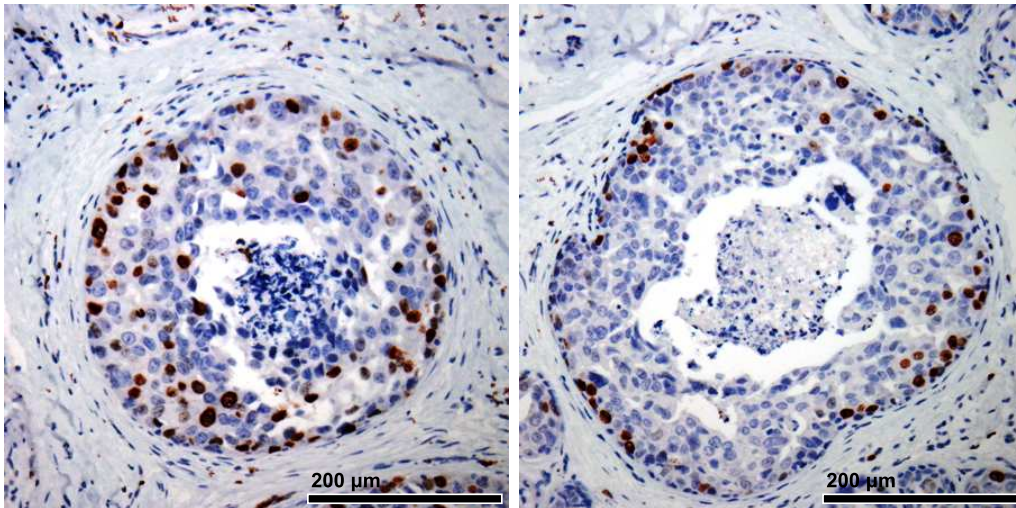


Fig. 7. Ki-67 immunohistochemistry for ducts F3 (left) and F19 (right) for anonymised case 100019. Ki-67 positive nuclei stain dark red; Ki-67 negative nuclei are counterstained light blue. A colour verison of this image is available online.

We now test this hypothesis based upon a careful analysis of Ki-67 immunohistochemistry in two exemplar ducts (F3 and F19) for a DCIS patient (anonymised case 100019) (Edgerton et al., 2011). See Fig. 7. For each of these ducts, we calculate the distance of all nuclei and Ki-67 positive nuclei to the duct wall, the mean distance from the duct centroid to the duct wall (i.e., the radius $R_{\mathrm{duct}}$), and the mean duct viable rim thickness $T$. Next, we create a histogram of Ki-67-positive nucleus distances to the duct wall (Fig. 8, first row), all nucleus distances to the duct wall *using the same histogram "bins"* (Fig. 8, second row), and divide these to obtain the proliferative index (PI) versus distance from the duct wall (Fig. 8, third row).

Next, we estimate the 3-D steady-state oxygen profile through the ducts (assumed radially symmetric with no variation in the longitudinal direction):

$$0 = L^2 \left( \sigma'' + \frac{1}{r} \sigma' \right) - \sigma, \quad 0 < r < R_{\mathrm{duct}} \tag{37}$$

with boundary conditions

$$\sigma(R_{\mathrm{duct}} - T) = \sigma_{\mathrm{H}}, \qquad \sigma'(0) = 0, \tag{38}$$
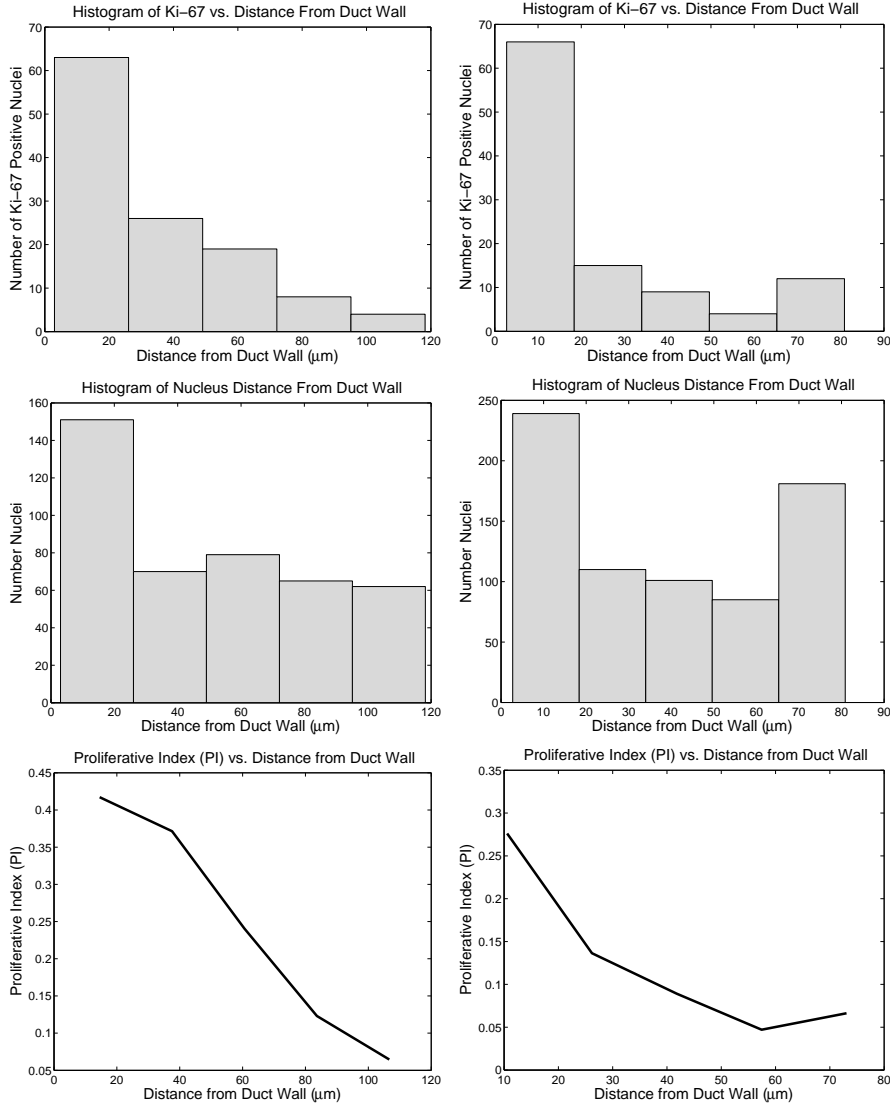
26

Fig. 8. Histograms of Ki-67 positive nuclei vs. distance from duct wall (top row), all nuclei vs. distance from duct wall (middle row), and proliferative index vs. distance from the duct wall (bottom row). *Left column:* Duct F3. *Right column:* Duct F19.

The solution is

$$\sigma(r) = \frac{\sigma_{\mathrm{H}}}{I_0\left(\frac{R_{\mathrm{duct}}-T}{L}\right)} I_0\left(\frac{r}{L}\right), \tag{39}$$

where $I_n$ is the $n^{\mathrm{th}}$-order modifed Bessel function of the first kind, $\sigma$ is nondimensionalised by the normoxic oxygen level in non-pathological tissue, $L = 100\,\mu\mathrm{m}$, and $\sigma_{\mathrm{H}} = 0.2$. (See Part II.) The mean value of the oxygen solution in the viable rim ($R_{\mathrm{duct}} - T < r < R_{\mathrm{duct}}$) is given explicitly by

$$\langle\sigma\rangle = \left(\frac{2L\sigma_{\mathrm{H}}}{2R_{\mathrm{duct}}T - T^2}\right)\left(\frac{R_{\mathrm{duct}}I_1\left(\frac{R_{\mathrm{duct}}}{L}\right) - (R_{\mathrm{duct}} - T)\,I_1\left(\frac{R_{\mathrm{duct}}-T}{L}\right)}{I_0\left(\frac{R_{\mathrm{duct}}-T}{L}\right)}\right). \tag{40}$$

27

For the duct in F3,

$$R_{\text{duct}} \approx 188.4634\,\mu\text{m}, \qquad T \approx 119.0256\,\mu\text{m}, \qquad \text{and} \qquad \langle\sigma\rangle \approx 0.282145,$$

and for the duct in F19,

$$R_{\text{duct}} \approx 217.5548\,\mu\text{m}, \qquad T \approx 97.9602\,\mu\text{m}, \qquad \text{and} \qquad \langle\sigma\rangle \approx 0.280459.$$
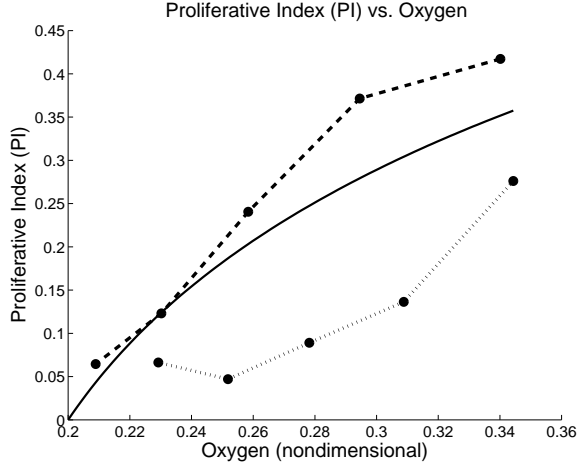


Fig. 9. Comparison of the predicted PI curve (solid curve) with data from duct F3 (dashed curve) and duct F19 (dotted curve) for case 100019.

By correlating the oxygen solutions with the PI profiles, we estimate the relationship between the measured PI and $\sigma$ in the ducts. We plot these curves for F3 (dashed curve) and F19 (dotted curve) against the predicted curve (solid curve) from Macklin et al. (2009a) in Fig. 9. The theoretical predictions and measurements agree qualitatively but not quantitatively. We conclude that while proliferation correlates with oxygen levels throughout the tumour, oxygenation alone cannot fully determine PI. Hence, there must be additional heterogeneities in other microenvironmental factors (e.g., EGF), gene expression, or protein signalling across the tumour.

The next natural question is whether we can account for these heterogeneities with our current functional form by applying the same analysis to the individual ducts. We use AI = 0.008838 in each duct, and PI, $R_{\text{duct}}$, and $T$ as measured separately for each duct above. For the duct in F3,

$$\text{PI} = 0.281030, \qquad \alpha_{\text{A}} \approx 0.00162405\,\text{h}^{-1},$$
$$\langle\alpha_{\text{P}}\rangle \approx 0.0277579\,\text{h}^{-1}, \qquad \text{and} \qquad \overline{\alpha}_P(\mathcal{S}, \bullet) \approx 0.270331\,\text{h}^{-1};$$
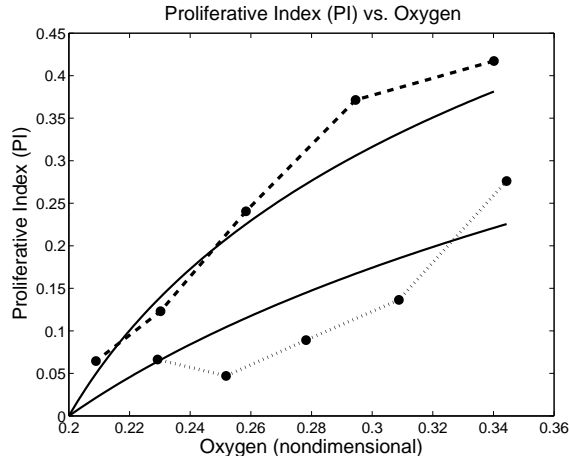
and for the duct in F19,

Fig. 10. Comparison of the hypothesised (solid) and measured (dashed and dotted) PI vs. $\sigma$ curves for duct F3 (dashed) duct F19 (dotted).

$$\text{PI} = 0.148045, \qquad \alpha_A \approx 0.00129067\,\text{h}^{-1},$$
$$\langle \alpha_P \rangle \approx 0.0110190\,\text{h}^{-1}, \qquad \text{and} \qquad \overline{\alpha_P}(\mathcal{S}, \bullet) \approx 0.109562\,\text{h}^{-1}.$$

Using this, we generate PI-vs-$\sigma$ curves for the individual ducts based upon Eq. 33 and compare them to the measured data in Fig. 10. There is generally much improved quantitative agreement between the predicted (solid) and measured (dashed and dotted) curves. The difference in the predicted curves for the two ducts is due to the substantial difference in $\overline{\alpha}_P$: $\overline{\alpha}_P$ is much greater for F3, which has the overall higher PI curve.

We next examine the data in the ducts (Fig. 7) within the context of our modelling framework and the predicted PI-vs-$\sigma$ curves to generate additional biological hypotheses. Notice that the cell density is lower in F3 (Fig. 7 left: larger nuclei with greater spacing between cells) than in F19 (Fig. 7 right: smaller nuclei with less spacing between cells). These lead us to hypothesise that $\overline{\alpha}_P$ decreases with increasing cell density. E-cadherin/$\beta$-catenin signalling may be the physiological explanation of the phenomenon: when E-cadherin is bound to E-cadherin on a neighboring cell, $\beta$-catenin binds to the phosphorylated receptors, blocking its downstream pro-proliferative activity. (See Section 1.1.) For higher cell densities, more cell surfaces are in contact with each other, providing greater opportunities for E-cadherin binding; we consequently hypothesise that cell density correlates with cell cycle blockade by the E-cadherin/$\beta$-catenin pathway, resulting in the apparent relationship between cell density and $\overline{\alpha}_P$. Further evidence can be seen in duct F19 (Fig. 7, right): the majority of the proliferation activity is in a single layer of cells along the duct wall. Because these cells are adhered to the basement membrane, they present less surface for E-cadherin binding activity (relative to the interior cells), resulting in reduced E-cadherin blockade of proliferation.

These hypotheses can be tested by correlating $\overline{\alpha}_P$ with cell density in a larger

number of ducts, performing IHC for $\beta$-catenin activity, and correlating $\beta$-catenin-mediated transcription (indicated by presence of $\beta$-catenin in the nuclei) with cell density and distance from the duct wall. One could use these data to hypothesise, calibrate, and test new functional forms for $\alpha_P$, such as:

$$\alpha_P(\mathcal{S}, \sigma, \bullet, \circ) = \overline{\alpha}_P(\bullet, \circ) \left( 1 - \mathcal{E}\langle\mathcal{E}\rangle \frac{\rho}{\rho_{\max}} \right) \left( \frac{\sigma - \sigma_H}{1 - \sigma_H} \right), \qquad (41)$$

where $\rho$ is the local cell density, PI $\approx 0$ when $\rho = \rho_{\max}$, $\mathcal{E}$ is the cell's (nondimensional) E-cadherin expression, and $\langle\mathcal{E}\rangle$ is the tumour's mean E-cadherin expression. In such a formulation, $\overline{\alpha}_P(\bullet, \circ)$ determines the cell's $\mathcal{Q} \to \mathcal{P}$ transition rate in normoxic conditions with minimal E-cadherin signalling.

## 5  Discussion and Looking Forward

In this work, we developed and analysed an agent-based model of ductal carcinoma in situ (DCIS) of the breast. Our work refines and makes more explicit the biological underpinnings of current agent-based cell models, particularly regarding finite cell-cell interaction distances, the need for partial cell overlap to account for uncertainty in cell positions and morphology, and a more rigorous way to vary phenotypic transition probabilities with the time step size, the cell's internal state, and the microenvironment. We provide the most detailed model to date of cell necrosis, and are the first to model cell calcification. Our analysis of the model steady-state, volume-veraged dynamics lead to quantitative predictions on the relationship between cell proliferation, oxygen availability, and cell signalling heterogeneity; these predictions were tested against actual patient data, yielding further insight on DCIS biology.

In Part II (Macklin et al., 2011), we use this analysis to develop a patient-specific calibration protocol, which is broadly applicable to well-formulated agent-based models. We test this protocol using data from an actual DCIS patient to simulate DCIS in 1.5 mm length of breast duct for 45 days. The simulation results will lead to quantitative predictions on the rate of DCIS growth (approximately 1 cm/year), which we shall validate against independent clinical data. The model will predict a (linear) relationship between the size of a calcification (as measured pre-operatively in a mammogram) and the actual tumour size (as measured post-operatively by a pathologist)–this, too, is successfully validated against a large set of clinical data. Lastly, the model will yield new insight on the biological and biomechanical underpinnings of the growing body of statistical knowledge that has been accumulated on DCIS, raising the possibilty of improved clinical planning and treatment of DCIS.

## Acknowledgements

## References

R. G. Abbott, S. Forrest, and K. J. Pienta. Simulating the hallmarks of cancer. *Artif. Life*, 12(4):617–34, 2006. doi: 10.1162/artl.2006.12.4.617.

T. L. Adamovich and R. M. Simmons. Ductal carcinoma in situ with microinvasion. *Am. J. Surg.*, 186(2):112–6, 2003. doi: 10.1016/S0002-9610(03)00166-1.

L. Ai, W.-J. Kim, T.-Y. Kim, C. R. Fields, N. A. Massoll, K. D. Robertson, and K. D. Brown. Epigenetic silencing of the tumor suppressor cystatin m occurs during breast cancer progression. *Canc. Res.*, 66(16):7899–909, 2006. doi: 10.1158/0008-5472.CAN-06-0576.

American Cancer Society. American cancer society breast cancer facts and figures 2007-2008. *Atlanta: American Cancer Society, Inc.*, 2007.

E. Anderson. Cellular homeostasis and the breast. *Maturitas*, 48(S1):13–7, 2004. doi: 10.1016/j.maturitas.2004.02.010.

A. Bankhead III, N. S. Magnuson, and R. B. Heckendorn. Cellular automaton simulation examining progenitor heirarchy structure effects on mammary ductal carcinoma *in situ*. *J. Theor. Biol.*, 246(3):491–8, 2007. doi: 10.1016/j.jtbi.2007.01.011.

L. F. Barros, T. Hermosilla, and J. Castro. Necrotic volume increase and the early physiology of necrosis. *Comp. Biochem. Physiol. A. Mol. Integr. Physiol.*, 130(3):401–9, 2001. doi: 10.1016/S1095-6433(01)00438-X.

F. O. Baxter, K. Neoh, and M. C. Tevendale. The beginning of the end: Death signaling in early involution. *J. Mamm. Gland Biol. Neoplas.*, 12(1):3–13, 2007. doi: 10.1007/s10911-007-9033-9.

E. L. Bearer, J. S. Lowengrub, Y.-L. Chuang, H. B. Frieboes, F. Jin, S. M. Wise, M. Ferrari, D. B. Agus, and V. Cristini. Multiparameter computational modeling of tumor invasion. *Cancer Res.*, 69(10):4493–501, 2009. doi: 10.1158/0008-5472.CAN-08-3834.

L. M. Butler, S. Khan, G. E. Rainger, and G. B. Nash. Effects of endothelial basement membrane on neutrophil adhesion and migration. *Cell. Immun.*, 251(1):56–61, 2008. doi: 10.1016/j.cellimm.2008.04.004.

H. M. Byrne and D. Drasdo. Individual-based and continuum models of growing cell populations: A comparison. *J. Math. Biol.*, 58(4–5):657–87, 2009. doi: 10.1007/s00285-008-0212-0.

N. Cabioglu, K. K. Hunt, A. A. Sahin, H. M. Kuerer, G. V. Babiera, S. E. Singletary, G. J. Whitman, M. I. Ross, F. C. Ames, B. W. Feig, T. A. Buchholz, and F. Meric-Bernstam. Role for intraoperative margin assessment in patients undergoing breast-conserving surgery. *Ann. Surg. Oncol.*, 14(4): 1458–71, 2007. doi: 10.1245/s10434-006-9236-0.

L. L. Chen, L. Zhang, J. Yoon, and T. S. Deisboeck. Cancer cell motility: optimizing spatial search strategies. *Biosys.*, 95(3):234–42, 2009a. doi: 10.1016/j.biosystems.2008.11.001.

W. W. Chen, B. Schoeberl, P. J. Jasper, M. Niepel, U. B. Nielsen, D. A. Lauffenburger, and P. K. Sorger. Input-output behavior of ErbB signaling pathways as revealed by a mass action model trained against dynamic data. *Mol. Syst. Biol.*, 5(1):239ff, 2009b. doi: 10.1038/msb.2008.74.

L. Cheng, N. K. Al-Kaisi, N. H. Gordon, A. Y. Liu, F. Gebrail, and R. R. Shenk. Relationship between the size and margin status of ductal carcinoma in situ of the breast and residual disease. *J. Natl. Cancer Inst.*, 89(18):1356–60, 1997.

S. Ciatto, S. Bianchi, and V. Vezzosi. Mammographic appearance of calcifications as a predictor of intraductal carcinoma histologic subtype. *Eur. Radiology*, 4(1):23–6, 1994. doi: 10.1007/BF00177382.

M. Conacci-Sorrell, J. Zhurinsky, and A. Ben-Zeév. The cadherin-catenin adhesion system in signaling and cancer. *J. Clin. Invest.*, 109(8):987–91, 2002. doi: 10.1172/JCI15429.

V. Cristini and J. Lowengrub. *Multiscale modeling of cancer.* Cambridge University Press, Cambridge, UK, 2010. ISBN 978-0521884426.

V. Cristini, J. S. Lowengrub, and Q. Nie. Nonlinear simulation of tumor growth. *J. Math. Biol.*, 46(3):191–224, 2003. doi: 10.1007/s00285-002-0174-6.

J. C. Dallon and H. G. Othmer. How cellular movement determines the collective force generated by the dictyostelium discoideum slug. *J. Theor. Biol.*,

231(2):203–22, 2004. doi: 10.1016/j.jtbi.2004.06.015.

C. G. Danes, S. L. Wyszomierski, J. Lu, C. L. Neal, W. Yang, and D. Yu. 14-3-3$\zeta$ down-regulates p53 in mammary epithelial cells and confers luminal filling. *Canc. Res.*, 68(6):1760–7, 2008. doi: 10.1158/0008-5472.CAN-07-3177.

T. S. Deisboeck, Z. Wang, P. Macklin, and V. Cristini. Multiscale cancer modeling. *Annu. Rev. Biomed. Eng.*, 2010. (in review).

M. F. Dillon, E. W. McDermott, A. O'Doherty, C. M. Quinn, A. D. Hill, and N. O'Higgins. Factors affecting successful breast conservation for ductal carcinoma in situ. *Ann. Surg. Oncol.*, 14(5):1618–28, 2007. doi: 10.1245/s10434-006-9246-y.

S. Dormann and A. Deutsch. Modeling of self-organized avascular tumor growth with a hybrid cellular automaton. *In Silico Biology*, 2(3):393–406, 2002.

D. Drasdo. Coarse graining in simulated cell populations. *Adv. Complex Sys.*, 8(2 & 3):319–63, 2005. doi: 10.1142/S0219525905000440.

D. Drasdo and S. Höhme. Individual-based approaches to birth and death in avascular tumors. *Math. Comput. Modelling*, 37(11):1163–75, 2003.

D. Drasdo and S. Höhme. A single-scale-based model of tumor growth *in vitro*: monolayers and spheroids. *Phys. Biol.*, 2(3):133–47, 2005. doi: 10.1088/1478-3975/2/3/001.

D. Drasdo, R. Kree, and J. S. McCaskill. Monte-carlo approach to tissue cell populations. *Phys. Rev. E*, 52(6):6635–57, 1995. doi: 10.1103/PhysRevE.52.6635.

M. E. Edgerton, P. Macklin, Y.-L. Chuang, G. Tomaiuolo, W. Yang, J. Kim, A. K. K. L. Kumar, S. Sanga, A. D. M. Broom, A. Segura, S. Kaliki, K.-A. Do, and V. Cristini. An application of a multiscale mathematical modeling framework of ductal carcinoma in situ. *PLoS Med.*, 2011. (submitted).

A. W. El-Kareh and T. W. Secomb. A mathematical model for cisplatin cellular pharmacodynamics. *Neoplasia*, 5(2):161–9, 2003.

A. W. El-Kareh and T. W. Secomb. Two-mechanism peak concentration model for cellular pharmacodynamics of doxorubicin. *Neoplasia*, 7(7):705–13, 2005.

H. Enderling, A. R. A. Anderson, M. A. J. Chaplain, A. J. Munro, and J. S. Vaidya. Mathematical modelling of radiotherapy strategies for early breast cancer. *J. Theor. Biol.*, 241(1):158–71, 2006. doi: 10.1016/j.jtbi.2005.11.015.

H. Enderling, M. A. J. Chaplain, A. R. A. Anderson, and J. S. Vaidya. A mathematical model of breast cancer development, local treatment and recurrence. *J. Theor. Biol.*, 246:245–259, 2007.

B. Erbas, E. Provenzano, J. Armes, and D. Gertig. The natural history of ductal carcinoma *in situ* of the breast: a review. *Breast Canc. Res. Treat.*, 97(2):135–44, 2006. doi: 10.1007/s10549-005-9101-z.

S. J. Franks, H. M. Byrne, J. R. King, J. C. E. Underwood, and C. E. Lewis. Modelling the early growth of ductal carcinoma in situ of the breast. *J. Math. Biol.*, 47(5):424–452, 2003a. doi: 10.1007/s00285-003-0214-x.

S. J. Franks, H. M. Byrne, H. Mudhar, J. C. E. Underwood, and C. E. Lewis. Modelling the growth of comedo ductal carcinoma in situ. *Math. Med. Biol.*, 20(3):277–308, 2003b. doi: 10.1093/imammb/20.3.277.

S. J. Franks, H. M. Byrne, J. C. E. Underwood, and C. E. Lewis. Biological inferences from a mathematical model of comedo ductal carcinoma in situ of the breast. *J. Theor. Biol.*, 232(4):523–43, 2005. doi: 10.1016/j.jtbi.2004.08.032.

H. B. Frieboes, J. S. Lowengrub, S. Wise, X. Zheng, P. Macklin, E. L. Bearer, and V. Cristini. Computer simulations of glioma growth and morphology. *NeuroImage*, 37(S1):S59–S70, 2007. doi: 10.1016/j.neuroimage.2007.03.008.

J. Galle, M. Loeffler, and D. Drasdo. Modeling the effect of deregulated proliferation and apoptosis on the growth dynamics of epithelial cell populations in vitro. *Biophys. J.*, 88(1):62–75, 2005. doi: 10.1529/biophysj.104.041459.

J. Galle, M. Hoffmann, and G. Aust. From single cells to tissue architecture-a bottom-up approach to modelling the spatio-temporal organisation of complex multi-cellular systems. *J. Math. Biol.*, 58(1–2):261–83, 2009. doi: 10.1007/s00285-008-0172-4.

R. A. Gatenby, K. Smallbone, P. K. Maini, F. Rose, J. Averill, R. B. Nagle, L. Worrall, and R. J. Gillies. Cellular adaptations to hypoxia and acidosis during somatic evolution of breast cancer. *Br. J. Cancer*, 97(5):646–53, 2007. doi: 10.1038/sj.bjc.6603922.

F. G. Giancotti and E. Ruoslahti. Integrin signaling. *Science*, 285(5430): 1028–32, 1999. doi: 10.1126/science.285.5430.1028.

J. A. Glazier and F. Garner. Simulation of the differential adhesion driven rearrangement of biological cells. *Phys. Rev. E*, 47(3):2128–54, 1993. doi: 10.1103/PhysRevE.47.2128.

J. J. Going and T. J. Mohun. Human breast duct anatomy, the 'sick lobe' hypothesis and intraductal approaches to breast cancer. *Breast. Canc. Res. and Treat.*, 97(3):0167–6806, 2006. doi: 10.1007/s10549-005-9122-7.

N. S. Gov and A. Gopinathan. Dynamics of membranes driven by actin polymerization. *Biophys. J.*, 90(2):454–69, 2006. doi: 10.1529/biophysj.105.062224.

F. Graner and J. A. Glazier. Simulation of biological cell sorting using a two-dimensional extended potts model. *Phys. Rev. Lett.*, 69(13):2013–6, 1992. doi: 10.1103/PhysRevLett.69.2013.

D. Hanahan and R. A. Weinberg. The hallmarks of cancer. *Cell*, 100(1):57–70, 2000. doi: 10.1016/S0092-8674(00)81683-9.

R. K. Hansen and M. J. Bissell. Tissue architecture and breast cancer: the role of extracellular matrix and steroid hormones. *Endocrine-Related Cancer*, 7 (2):95–113, 2000. doi: 10.1677/erc.0.0070095.

S. Hoehme and D. Drasdo. Biomechanical versus nutrient control: what determines the growth dynamics of mammalian cell populations. 17(3):166–87, 2010. doi: 10.1080/08898480.2010.491032.

D. Ilić, E. A. Almeida, D. D. Schlaepfer, P. Dazin, S. Aizawa, and C. H. Damsky. Extracellular matrix survival signals transduced by focal adhesion

kinase suppress p53-mediated apoptosis. *J. Cell Biol.*, 143(2):547–60, 1998. doi: 10.1083/jcb.143.2.547.

A. Jemal, R. Siegel, E. Ward, T. Murray, J. Xu, and M. J. Thun. Cancer statistics, 2007. *CA Cancer J. Clin.*, 57(1):43–66, 2007. doi: 10.3322/canjclin.57.1.43.

T. X. Jiang and C. M. Chuong. Mechanism of skin morphogenesis I: Analyses with antibodies to adhesion molecules tenascin, NCAM, and integrin. *Dev. Biol.*, 150(1):82–98, 1992. doi: 10.1016/0012-1606(92)90009-6.

K. Kerlikowske, A. Molinaro, I. Cha, B. M. Ljung, V. L. Ernster, K. Stewart, K. Chew, D. H. Moore 2nd, and F. Waldman. Characteristics associated with recurrence among women with ductal carcinoma in situ treated by lumpectomy. *J. Natl. Cancer Inst.*, 95(22):1692–702, 2003. doi: 10.1093/jnci/djg097.

S. Khan, M. Rogers, K. Khurana, M. Meguid, and P. Numann. Estrogen receptor expression in benign breast epithelium and breast cancer risk. *J. Natl. Canc. Inst.*, 90(1):37–42, 1998.

S. Khan, A. Sachdeva, S. Naim, M. Meguid, W. Marx, H. Simon, et al. The normal breast epithelium of women with breast cancer displays an aberrant response to estradiol. *Canc. Epidemiol. Biomarkers Prev.*, 8:867–72, 1999.

S. Kharait, S. Hautaniemi, S. Wu, A. Iwabu, D. A. Lauffenburger, and A. Wells. Decision tree modeling predicts effects of inhibiting contractility signaling on cell motility. *BMC Syst. Biol.*, 1:9ff, 2007. doi: 10.1186/1752-0509-1-9.

O. T. Lampejo, D. M. Barnes, P. Smith, and R. R. Millis. Evaluation of infiltrating ductal carcinomas with a DCIS component: correlation of the histologic type of the in situ component with grade of the infiltrating component. *Semin. Diagn. Pathol.*, 11(3):215–22, 1994.

J. S. Lowengrub, H. B. Frieboes, F. Jin, Y.-L. Chuang, X. Li, P. Macklin, S. M. Wise, and V. Cristini. Nonlinear modeling of cancer: Bridging the gap between cells and tumors. *Nonlinearity*, 23(1):R1–R91, 2010. doi: 10.1088/0951-7715/23/1/R01.

P. J. Lucio, M. T. Faria, A. M. Pinto, M. R. da Silva, M. E. Correia Jr., R. J. da Costa, and A. B. Parreira. Expression of adhesion molecules in chronic B-cell lymphoproliferative disorders. *Haematologica*, 83(2):104–11, 1998.

P. Macklin. Biological background. Cristini and Lowengrub (2010), chapter 2, pages 8–24. ISBN 978-0521884426.

P. Macklin and J. S. Lowengrub. Evolving interfaces via gradients of geometry-dependent interior poisson problems: application to tumor growth. *J. Comput. Phys.*, 203(1):191–220, 2005. doi: 10.1016/j.jcp.2004.08.010.

P. Macklin and J. S. Lowengrub. An improved geometry-aware curvature discretization for level set methods: application to tumor growth. *J. Comput. Phys.*, 215(2):392–401, 2006. doi: 10.1016/j.jcp.2005.11.016.

P. Macklin and J. S. Lowengrub. Nonlinear simulation of the effect of microenvironment on tumor growth. *J. Theor. Biol.*, 245(4):677–704, 2007. doi: 10.1016/j.jtbi.2006.12.004.

P. Macklin and J. S. Lowengrub. A new ghost cell/level set method for moving boundary problems: Application to tumor growth. *J. Sci. Comp.*, 35(2–3): 266–99, 2008. doi: 10.1007/s10915-008-9190-z.

P. Macklin, J. Kim, G. Tomaiuolo, M. E. Edgerton, and V. Cristini. Agent-based modeling of ductal carcinoma in situ: Application to patient-specific breast cancer modeling. In Pham (2009), chapter 4, pages 77–112. ISBN 978-1-4419-0810-0.

P. Macklin, S. McDougall, A. R. A. Anderson, M. A. J. Chaplain, V. Cristini, and J. Lowengrub. Multiscale modeling and nonlinear simulation of vascular tumour growth. *J. Math. Biol.*, 58(4–5):765–98, 2009b. doi: 10.1007/s00285-008-0216-9.

P. Macklin, M. E. Edgerton, and V. Cristini. Agent-based cell modeling: application to breast cancer. Cristini and Lowengrub (2010), chapter 10, pages 216–244. ISBN 978-0521884426.

P. Macklin, M. E. Edgerton, J. Lowengrub, and V. Cristini. Discrete cell modeling. Cristini and Lowengrub (2010), chapter 6, pages 92–126. ISBN 978-0521884426.

P. Macklin, M. E. Edgerton, and V. Cristini. Patient-calibrated agent-based modelling of ductal carcinoma in situ (DCIS) II: From microscopic measurements to macroscopic predictions of clinical progression. *J. Theor. Biol.*, 2011. (in review).

K. D. Mannes, M. E. Edgerton, J. F. Simpson, R. A. Jenson, and D. L. Page. Pagetoid spread in ductal carcinoma in situ: Characterization and computer simulation. In *United States and Canadian Academy of Pathology (USCAP) Annual Meeting 2002*, Chicago, 2002.

D. F. Moffat and J. J. Going. Three dimensional anatomy of complete duct systems in human breast: pathological and developmental implications. *J. Clin. Pathol.*, 49(1):48–52, 1996. doi: 10.1136/jcp.49.1.48.

K.-A. Norton, M. Wininger, G. Bhanot, S. Ganesan, N. Barnard, and T. Shinbrot. A 2D mechanistic model of breast ductal carcinoma in situ (DCIS) morphology and progression. *J. Theor. Biol.*, 263(4):393–406, 2010. doi: 10.1016/j.jtbi.2009.11.024.

T. Ohtake, I. Kimijima, T. Fukushima, M. Yasuda, K. Sekikawa, S. Takenoshita, and R. Abe. Computer-assisted complete three-dimensional reconstruction of the mammary ductal/lobular systems. *Cancer*, 91 (12):2263–72, 2001. doi: 10.1002/1097-0142(20010615)91:12<2263::AID-CNCR1257>3.0.CO;2-5.

M. R. Owen, H. M. Byrne, and C. E. Lewis. Mathematical modelling of the use of macrophages as vehicles for drug-delivery to hypoxic tumour sites. *J. Theor. Biol.*, 226(4):377–391, 2004. doi: 10.1016/j.jtbi.2003.09.004.

D. L. Page. The clinical significance of mammary epithelial hyperplasia. *Breast*, 1(1):3–7, 1992. doi: 10.1016/0960-9776(92)90003-K.

D. L. Page, W. D. Dupont, L. W. Rogers, and M. Landenberger. Intraductal carcinoma of the breast: follow-up after biopsy only. *Cancer*, 49(4):751–8, 1982. doi: 10.1002/1097-0142(19820215)49:4<751::AID-

CNCR2820490426>3.0.CO;2-Y.

P. Panorchan, M. S. Thompson, K. J. Davis, Y. Tseng, K. Konstantopoulos, and D. Wirtz. Single-molecule analysis of cadherin-mediated cell-cell adhesion. *J. Cell Sci.*, 119(1):66–74, 2006. doi: 10.1242/jcs.02719.

T. Pham, editor. *Computational Biology: Issues and Applications in Oncology.* Springer, New York, NY USA, 2009. ISBN 978-1-4419-0810-0.

I. Ramis-Conde, M. A. J. Chaplain, and A. R. A. Anderson. Mathematical modelling of cancer cell invasion of tissue. *Math. Comp. Model.*, 47(5–6): 533–545, 2008a. doi: 10.1016/j.mcm.2007.02.034.

I. Ramis-Conde, D. Drasdo, A. R. A. Anderson, and M. A. J. Chaplain. Modeling the influence of the e-cadherin-beta-catenin pathway in cancer cell invasion: A multiscale approach. *Biophys. J.*, 95(1):155–165, 2008b. doi: 10.1529/biophysj.107.114678.

K. A. Rejniak. An immersed boundary framework for modeling the growth of individual cells: An application to the early tumour development. *J.Theor. Biol.*, 247(1):186–204, 2007. doi: 10.1016/j.jtbi.2007.02.019.

K. A. Rejniak and A. R. A. Anderson. A computational study of the development of epithelial acini: I. sufficient conditions for the formation of a hollow structure. *Bull. Math. Biol.*, 70(3):677–712, 2008a. doi: 10.1007/s11538-007-9274-1.

K. A. Rejniak and A. R. A. Anderson. A computational study of the development of epithelial acini: II. necessary conditions for structure and lumen stability. *Bull. Math. Biol.*, 70(5):1450–79, 2008b. doi: 10.1007/s11538-008-9308-3.

K. A. Rejniak and R. H. Dillon. A single cell-based model of the ductal tumor microarchitecture. *Comp. Math. Meth. Med.*, 8(1):51–69, 2007. doi: 10.1080/17486700701303143.

K. Rennstam and I. Hedenfalk. High-throughput genomic technology in research and clinical management of breast cancer. molecular signatures of progression from benign epithelium to metastatic breast cancer. *Breast Canc. Res.*, 8(4):213ff, 2006. doi: 10.1186/bcr1528.

B. Ribba, O. Saut, T. Colin, D. Bresch, E. Grenier, and J. P. Boissel. A multiscale mathematical model of avascular tumor growth to investigate the therapeutic benefit of anti-invasive agents. *J. Theor. Biol.*, 243(4):532–41, 2006. doi: 10.1016/j.jtbi.2006.07.013.

M. E. Sanders, P. A. Schuyler, W. D. Dupont, and D. L. Page. The natural history of low-grade ductal carcinoma in situ of the breast in women treated by biopsy only revealed over 30 years of long-term follow-up. *Cancer*, 103 (12):2481–4, 2005. doi: 10.1002/cncr.21069.

G. Schaller and M. Meyer-Hermann. Multicellular tumor spheroid in an off-lattice Voronoi-Delaunay cell model. *Phys. Rev. E*, 71(5):051910, 2005. doi: 10.1103/PhysRevE.71.051910.

B. I. Shraiman. Mechanical feedback as a possible regulator of tissue growth. *Proc. Natl. Acad. Sci. USA*, 102(9):3318–23, 2005. doi: 10.1073/pnas.0404782102.

A. S. Silva and R. A. Gatenby. A theoretical quantitative model for evolution of cancer chemotherapy resistance. *Biol. Direct*, 5(1):25ff, 2010. doi: 10.1186/1745-6150-5-25.

A. S. Silva, R. A. Gatenby, R. J. Gillies, and J. A. Yunes. A quantitative theoretical model for the development of malignancy in ductal carcinoma *in situ. J. Theor. Biol.*, 262(4):601–13, 2010. doi: 10.1016/j.jtbi.2009.10.031.

S. A. Silver and F. A. Tavassoli. Ductal carcinoma in situ with microinvasion. *Breast J.*, 4(5):344–8, 1998. doi: 10.1046/j.1524-4741.1998.450344.x.

M. J. Silverstein. Predicting residual disease and local recurrence in patients with ductal carcinoma in situ. *J. Natl. Cancer Inst.*, 89(18):1330–1, 1997.

M. J. Silverstein. Ductal carcinoma in situ of the breast. *Annu. Rev. Med.*, 51(1):17–32, 2000. doi: 10.1146/annurev.med.51.1.17.

P. T. Simpson, J. S. Reis-Filho, T. Gale, and S. R. Lakhani. Molecular evolution of breast cancer. *J. Pathol.*, 205(2):248–54, 2005. doi: 10.1002/path.1691.

K. Smallbone, R. A. Gatenby, R. J. Gillies, P. K. Maini, and D. J. Gavaghan. Metabolic changes during carcinogenesis: Potential impact on invasiveness. *J. Theor. Biol.*, 244(2):703–713, 2007. doi: 10.1016/j.jtbi.2006.09.010.

J. A. Smith and L. Martin. Do cells cycle? *Proc. Natl. Acad. Sci. USA*, 70: 1263–67, 1973. URL http://www.pnas.org/content/70/4/1263.

L. Sontag and D. E. Axelrod. Evaluation of pathways for progression of heterogeneous breast tumors. *J. Theor. Biol.*, 232(2):179–89, 2005. doi: 10.1016/j.jtbi.2004.08.002.

T. A. Springer. Adhesion receptors of the immune system. *Nature*, 346(6283): 425–34, 1990. doi: 10.1038/346425a0.

P. C. Stomper and F. R. Margolin. Ductal carcinoma in situ: the mammographer's perspective. *Am. J. Roentgenology*, 162:585–91, 1994.

D. G. Stupack and D. A. Cheresh. Get a ligand, get a life: Integrins, signaling and cell survival. *J. Cell. Sci.*, 115(19):3729–38, 2002. doi: 10.1242/jcs.00071.

P. J. Tannis, O. E. Nieweg, R. A. Valdés Olmos, and B. B. R. Kroon. Anatomy and physiology of lymphatic drainage of the breast from the perspective of sentinel node biopsy. *J. Am. Coll. Surg.*, 192(3):399–409, 2001. doi: 10.1016/S1072-7515(00)00776-6.

M. J. Terol, M. Tormo, J. A. Martinez-Climent, I. Marugan, I. Benet, A. Ferrandez, A. Teruel, R. Ferrer, and J. Garcia-Conde. Soluble intercellular adhesion molecule-1 (s-ICAM-1/s-CD54) in diffuse large B-cell lymphoma: association with clinical characteristics and outcome. *Ann. Oncol.*, 14(3): 467–74, 2003. doi: 10.1093/annonc/mdg057.

A. Venkatesan, P. Chu, K. Kerlikowske, E. A. Sickles, and R. Smith-Bindman. Positive predictive value of specific mammographic findings according to reader and patient variables. *Radiology*, 250(3):648–57, 2009. doi: 10.1148/radiol.2503080541.

Z. Wang, L. Zhang, J. Sagotsky, and T. S. Deisboeck. Simulating non-small cell lung cancer with a multiscale agent-based model. *Theor. Biol. Med.*

*Model.*, 4:50ff, 2007. doi: 10.1186/1742-4682-4-50.

J. P. Ward and J. R. King. Mathematical modelling of avascular tumour growth. *IMA J. Math. Appl. Medicine Biol.*, 14(1):36–69, 1997. doi: 10.1093/imammb/14.1.39.

C. Wei, M. Larsen, M. P. Hoffman, and K. M. Yamada. Self-organization and branching morphogenesis of primary salivary epithelial cells. *Tissue Eng.*, 13(4):721–35, 2007. doi: 10.1089/ten.2006.0123.

S. R. Wellings, H. M. Jensen, and R. G. Marcum. An atlas of subgross pathology of the human breast with special reference to possible precancerous lesions. *J. Natl. Cancer Inst.*, 55(2):231–73, 1975.

S. M. Wise, J. S. Lowengrub, H. B. Frieboes, and V. Cristini. Three-dimensional multispecies nonlinear tumor growth–I. model and numerical method. *J. Theor. Biol.*, 253(3):524–43, 2008. doi: 10.1016/j.jtbi.2008.03.027.

L. Zhang, C. A. Athale, and T. S. Deisboeck. Development of a three-dimensional multiscale agent-based tumor model: simulating gene-protein interaction profiles, cell phenotypes and multicellular patterns in brain cancer. *J. Theor. Biol.*, 244(7):96–107, 2007. doi: 10.1016/j.jtbi.2006.06.034.

L. Zhang, Z. Wang, J. A. Sagotsky, and T. S. Deisboeck. Multiscale agent-based cancer modeling. *J. Math. Biol.*, 58(4–5):545–59, 2009. doi: 10.1007/s00285-008-0211-1.

## A   A simple family of potential functions

As in Drasdo et al. (1995); Drasdo and Höhme (2003, 2005); Drasdo (2005); Ramis-Conde et al. (2008a,b), and Byrne and Drasdo (2009), we use potential functions to model biomechanical interactions between cells and the microenvironment. We now define two potential functions $\varphi$ (for adhesion) and $\psi$ (for mechanical resistance/repulsion) used in the agent model. These potentials are updated from those presented in Macklin et al. (2009a, 2010a,b). A good discussion of the use of potential functions to mediate cell-cell interactions for individual-based models can be found in Byrne and Drasdo (2009). Recent work by Ramis-Conde et al. (2008a,b) ties potential functions to more detailed models of intracellular mechanics and E-cadherin dynamics.

For the adhesion potential $\varphi$, let $R_{\mathrm{A}}$ be the cell's maximum adhesive interaction distance. For any $n \in \mathbb{N}$, define $\varphi$ first by its gradient:

$$\nabla\varphi(\mathbf{r}; R_{\mathrm{A}}, n) = \begin{cases} \left(1 - \frac{|\mathbf{r}|}{R_{\mathrm{A}}}\right)^{n+1} \frac{\mathbf{r}}{|\mathbf{r}|}, & 0 \le |\mathbf{r}| \le R_{\mathrm{A}} \\ \mathbf{0} & \text{else,} \end{cases} \tag{A.1}$$

and so

$$\varphi(\mathbf{r}; R_{\mathrm{A}}, n) = \begin{cases} -\frac{R_{\mathrm{A}}}{n+2}\left(1 - \frac{|\mathbf{r}|}{R_{\mathrm{A}}}\right)^{n+2} & 0 \le |\mathbf{r}| \le R_{\mathrm{A}} \\ 0 & \text{else.} \end{cases} \tag{A.2}$$

Note that $\varphi$ and its derivatives have compact support, to model the finite interaction distance between cells; this is computationally beneficial as well (Macklin et al., 2009a, 2010b). The baseline case $n = 0$ is a linear ramping to the maximum force when $|\mathbf{r}| = 0$. For $n > 0$, $\varphi$ tapers off smoothly.

We apply $\varphi$ to the adhesive force imparted on cell $i$ by cell $j$ via

$$\mathbf{F}_{\mathrm{cca}}^{ij} = -\alpha_{\mathrm{cca}}\nabla\varphi\left(\mathbf{x}_j - \mathbf{x}_i; R_{\mathrm{A}}^i + R_{\mathrm{A}}^j, n_{\mathrm{cca}}^i\right). \tag{A.3}$$

Note that this takes into account the deformability of both cells by using $R_{\mathrm{A}}^i + R_{\mathrm{A}}^j$. When we apply $\varphi$ to cell-BM adhesion (as applied to cell $i$), we have

$$\mathbf{F}_{\mathrm{cba}}^i = -\alpha_{\mathrm{cba}}\nabla\varphi\left(d\left(\mathbf{x}_i\right)\mathbf{n}\left(\mathbf{x}_i\right); R_{\mathrm{A}}^i, n_{\mathrm{cba}}^i\right), \tag{A.4}$$

where $d\left(\mathbf{x_i}\right)$ is the distance of cell $i$ to the basement membrane, and the $\mathbf{n}\left(\mathbf{x}_i\right)$ is normal to the membrane (facing the epithelial side of the BM). Notice that setting the maximum interaction distance to $R_{\mathrm{A}}^i$ is consistent with our modelling simplification that the basement membrane is non-deformable.

Similarly, we define the repulsion potential $\psi$ through its gradient. If $m$ is a fixed nonnegative integer, $R_{\mathrm{N}}$ is the nuclear radius, $R$ is the cell's radius, and $M \ge 1$ is the cell's maximum repulsive force, define

$$\nabla\psi(\mathbf{r}; R_{\mathrm{N}}, R, M, m) = \begin{cases} -\left(c\frac{|\mathbf{r}|}{R_{\mathrm{N}}} + M\right)\frac{\mathbf{r}}{|\mathbf{r}|} & 0 \le |\mathbf{r}| \le R_{\mathrm{N}} \\ -\left(1 - \frac{|\mathbf{r}|}{R}\right)^{m+1}\frac{\mathbf{r}}{|\mathbf{r}|} & R_{\mathrm{N}} \le |\mathbf{r}| \le R \\ \mathbf{0} & \text{else,} \end{cases} \tag{A.5}$$

where

$$c = \left(\left(1 - \frac{R_{\mathrm{N}}}{R}\right)^{m+1} - M\right). \tag{A.6}$$

We can obtain $\psi$ by directly integrating $\nabla\psi$ with respect to $|\mathbf{x}|$ as we did for $\varphi$ (although it is not necessary for our model).

As with $\varphi$, $\psi$ and its derivatives have compact support; this models the fact that cells only repel one another when they are in physical contact. We make $\psi$ linear in the nuclear region (with $M \ge 1$) to model a stiffer material and allow the nuclear and cytoskeletal mechanics to be specified independently.

When we apply $\psi$ to the repulsive force imparted by cell $j$ on cell $i$, we have

$$\mathbf{F}_{\mathrm{ccr}}^{ij} = -\alpha_{\mathrm{ccr}}\nabla\psi\left(\mathbf{x}_j - \mathbf{x}_i; R_{\mathrm{N}}^i + R_{\mathrm{N}}^j, R^i + R^j, M_i, n_{\mathrm{ccr}}^i\right). \tag{A.7}$$
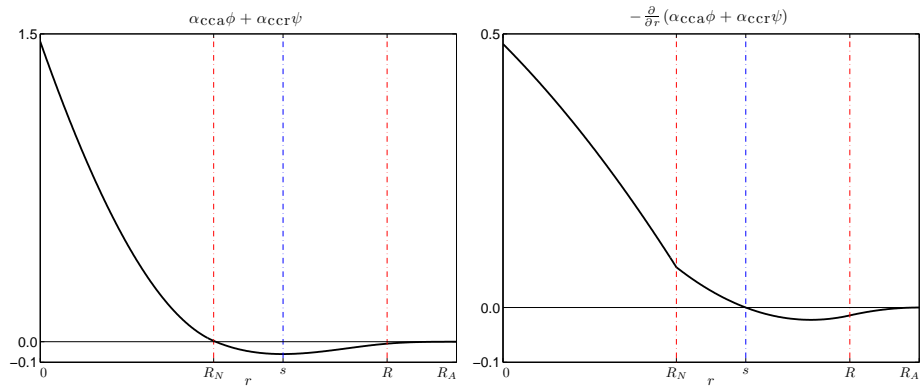
Fig. A.1. **Potential functions and derivatives** for $m = n = 1$, and $M = 1$, $\alpha_{\mathrm{ccr}} = 1$, and $\alpha_{\mathrm{cca}} = 0.5184$. <u>*Left*</u>: $\alpha_{\mathrm{ccr}}\psi + \alpha_{\mathrm{cca}}\varphi$. <u>*Right*</u>: $-\frac{\partial}{\partial r}(\alpha_{\mathrm{ccr}}\psi + \alpha_{\mathrm{cca}}\varphi)$.

When we apply $\psi$ to cell-BM repulsion (as applied to cell $i$), we have

$$\mathbf{F}_{\mathrm{cbr}}^{i} = -\alpha_{\mathrm{cbr}}\nabla\psi\left(d\left(\mathbf{x}_i\right)\mathbf{n}\left(\mathbf{x}_i\right); R_{\mathrm{N}}^{i}, R^{i}, M^{i}, n_{\mathrm{cbr}}^{i}\right). \tag{A.8}$$

In Fig. A.1, we plot $\alpha_{\mathrm{ccr}}\psi + \alpha_{\mathrm{cca}}\varphi$ and $-\frac{\partial}{\partial r}(\alpha_{\mathrm{ccr}}\psi + \alpha_{\mathrm{cca}}\varphi)$ for $\alpha_{\mathrm{ccr}} = 1$, $\alpha_{\mathrm{cca}} = 0.5184$, $R = 10$, $R_{\mathrm{A}} = 12$, $R_{\mathrm{N}} = 5$, $s = 7$, $M = 1$, and $n = m = 1$.